New Acid Medium Sol-Gel Synthesis of Metal Phosphates

by

Shanika Abeysooriya

A Thesis Presented in Partial Fulfillment
of the Requirements for the Degree
Master of Science

Approved November 2018 by the
Graduate Supervisory Committee:

Dong-Kyun Seo, Chair
Ryan J. Trovitch
Candace K. Chan

ARIZONA STATE UNIVERSITY

December 2018

ABSTRACT

New sol-gel routes based on peroxo complexes of early transition metals in a highly acidic medium were developed, to prepare metal oxide phosphates that feature structural protons. A sol-gel synthetic route was chosen because it allows atomic level mixing of precursors and lower heating temperatures, which are preferable in exploring metastable phases. Titanium and molybdenum sol-gel chemistries were the focus of the initial studies and the synthesis of $Ti_{1-x}Mo_xP_2O_7$ (x = 0 – 0.5) and $Mo_{1-y}Ti_yP_2O_{8-y}$ (y = 0 – 0.4) type metal oxide phosphates were explored. For the synthesis of the metal oxide phosphates, hydrogen peroxide was employed to prepare the respective precursor solutions. The peroxide ligand suppressed the immediate precipitation of metal cations in aqueous medium, by coordinating to Ti^{4+} and Mo^{6+} ions, and produced a soft wet-gel following polycondensation. Phosphoric acid was used to acidify the reaction medium and to provide protons and phosphate ions as structural components. From this synthetic route, a series of $Ti_{1-x}Mo_xP_2O_7$ (x = 0 – 0.5) and $Mo_{1-y}Ti_yP_2O_{8-y}$ (y = 0 – 0.4) crystalline compounds, with various degrees of purity, were synthesized. For x = 0 and y = 0, the crystalline compounds TiP_2O_7 and MoP_2O_8 were produced, respectively, after calcining at 600 °C.

In pursuit of new metastable molybdenum oxide phosphate compounds, peroxo-molybdenum precursor mixtures with different molar ratios were treated gently by low-temperature heating. After controlled drying in a lab oven, $MoO_2(H_2O)(HPO_4)$ crystals were obtained as a highly crystalline pure product instead of a gel. The dissolution of $MoO_2(H_2O)(HPO_4)$ in water and precipitation with a CsCl solution produced a new crystalline compound with a cubic unit cell (a = 11.8(2) Å). Further studies will lead to

crystal structure determination and elucidation of the aqueous chemistry of $MoO_2(H_2O)(HPO_4)$.

DEDICATION

To beloved family and friends for always guiding, supporting and standing by me.

"An idea that is developed and put into action is more important than an idea that exists only as an idea." – Lord Buddha

ACKNOWLEDGMENTS

I give great thanks to my advisor Dr. Dong-Kyun Seo, for his teachings, guidance and encouragement I would not have become a researcher without him. Thank you for always making time to provide feedback and suggestions, that helped me vastly improve my research skills.

I thank my family and friends for always supporting me in every possible way. Their advice and guidance as well as their faith in me was a pillar of strength.

TABLE OF CONTENTS

Page

CHAPTER Page

LIST OF TABLES

Table Page

LIST OF FIGURES

Figure Page

Figure Page

Figure Page

Figure Page

Figure Page

CHAPTER 1

INTRODUCTION

1.1 Sol-Gel Synthesis of Metal Oxides

The synthetic method explored in this study is sol-gel synthesis, which provides an opportunity to produce new metal compounds by forming a homogeneous hydrous metal oxide at a low temperature as an intermediate or final product. The low-temperature formation of metal compounds is in contrast to the traditional solid-state synthesis technique that has been commonly utilized to produce inorganic materials such as metal phosphates and pyrophosphates. In solid-state synthesis, the compounds are prepared simply by carefully mixing powder reactants, pelletizing and subsequent heating at a high temperature. While this synthetic route is easy to carry out, there are several drawbacks pertaining to this method.[1] Firstly, the diffusion of atoms and ions in reactant solids is slow and thus the reaction can become time-consuming or remain incomplete. Unreacted starting material may be found in the final product due to blockage of reactant diffusion and due to reactions that take place at the edges of adjacent particles.[1] Inability to control particle morphology is another issue that has been reported about solid-state synthesis. Two of the reported alternative synthetic routes for solid-state synthesis would be hydrothermal and sol-gel synthesis.[1]

Hydrothermal synthesis is utilized to synthesize crystalline materials directly from solutions, using single or heterogeneous phase reactions in an aqueous medium at temperatures greater than room temperature (even over 100 °C) and pressures greater than 0.9869 atm (even over 4935 atm) in autoclaves at various pH ranges.[1] While these syntheses allow the growth of crystalline compounds with melting points much higher than

the reaction temperatures, it consists of disadvantages such as usage of expensive autoclaves, potentially explosive conditions, and impossibility of observing crystal growth.[1]

In sol-gel synthesis, however, the formation of the sol-gel product occurs at ambient temperatures and pressures as the starting precursors are all dissolved in the solution from the start.[2] Other advantages that sol-gel synthesis provides are a greater control of particle size and morphology, and flexible synthetic conditions suitable for production of materials with high surface area and porosity.[2] **Figure 1.1** illustrates typical sol-gel processes where materials are synthesized by transforming precursor solutions to sol particles,

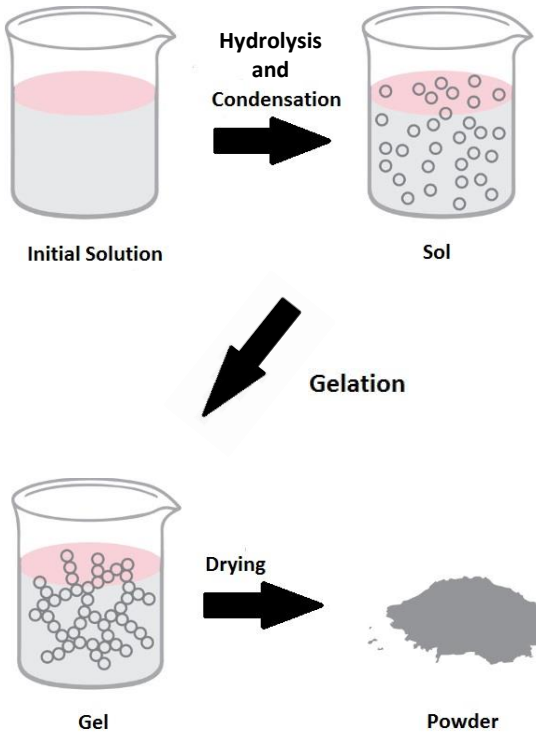

Figure 1.1 Schematic diagram of sol-gel process [Adapted from Ref. 2]

followed by formation of a three-dimensional network structure of the formed particles, called a gel.[2] The gel is then dried and optionally calcined to produce the final product.[2]

The International Union of Pure and Applied Chemistry (IUPAC) definition for a sol is "a fluid colloidal system of two or more components" as given in the IUPAC Goldbook.[3] Meanwhile, IUPAC defines a gel as a non-fluid colloidal network or polymer network that is expanded throughout its whole volume by a fluid.[4] In aqueous sol-gel synthesis of metal oxides, the formation of a sol occurs via hydrolysis and polycondensation of precursor molecules such as metal alkoxide precursors, especially for synthesis of silica gels and organically modified silicates (ORMOSILs).[2,5,6] Some examples of metal alkoxy ligands are methoxy ($-OCH_3$), ethoxy ($-OCH_2CH_3$), n-propoxy ($-O(CH_2)_2CH_3$) and n-butoxy ($-O(CH_2)_3CH_3$).[7] This process may continue and form monomers that further condense to cross-linked polymeric sol particulates. However, alkoxides of early transition metals are less popular because of their extremely fast hydrolysis and uncontrollable polycondensation. The disparity in hydrolysis rates of different metal alkoxides poses another obstacle in preparing homogeneous mixed metal oxides and introduction of organic groups into oxide materials.[7]

When transition metal precursors are hydrolyzed, the transition metal cations coordinate to ligands such as water and the electron density of the bonding $3a_1$ molecular orbital of the water molecule (σ donor) is transferred to the atomic orbitals (empty d orbitals) of the transition metals cation. When using highly polarized (high charge and smaller radius) metal cations such as Ti^{4+} and Mo^{6+}, the charge transfer strengthens the M–O (M: metal cation) bond and weakens the O–H bonds of the ligand water molecule, promoting hydrolysis.[8–11] Therefore, coordinated water molecules are stronger acids than

water molecules in the solvent, leading to an acidic solution as in the following reaction as an example:[11]

$$[M(OH_2)]^{z+} + H_2O \leftrightarrow [M-OH]^{(z-1)+} + H_3O^+ \qquad \textbf{eq. 1.1}$$

The acidity of the aquo ligand is directly dependent on the strength of the M–O bond. This may result in the metal cation being coordinated to three types of ligands: aquo (H_2O), hydroxo (HO^-) and oxo (O^{2-}).[11]

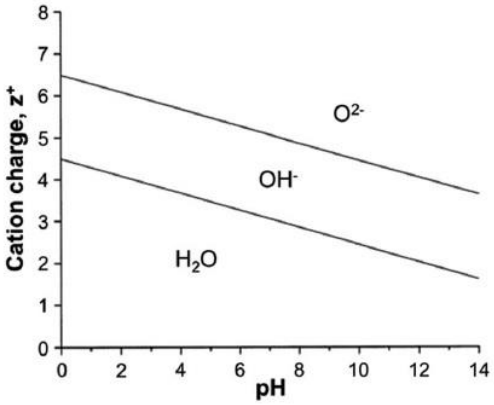

Figure 1.2 Relationship between charge, pH, and hydrolysis equilibrium of cations [Adapted from Ref. 10]

As depicted in **Figure 1.2**, therefore, the type of coordinated ligand varies, depending on the pH of the medium. During hydrolysis for Ti^{4+} and Mo^{6+} metal cations with strong M–O bonding; pH ranges from 13 – 14 and 4 – 13 respectively result in oxo ligand formation. Also, formation of hydro ligands is favored at pH ranges 4 – 13 and 0 – 4.[8–11]

The nature of the ligands is important in determining the condensation behavior of the metal complexes.[11] The aquo ligand doesn't act as a leaving group, as it has no

nucleophilic character. Therefore, a water molecule in M–OH_2 can't undergo condensation reactions. To the contrary, oxo ligands are better nucleophiles.[11] Due to the strong π character in the M–O bond of the oxo species, however, the nucleophilic strength of the oxygen atom is reduced, preventing oxo ligands from acting as a leaving group. Therefore, purely oxo species can't undergo condensation reactions.[11] In species such as $[M(OH)_h(OH_2)_{N-h}]^{(z-h)+}$ where both OH^- ligands and H_2O ligands are present, the hydroxo ligand will act as a nucleophile while the aquo ligand would act as a leaving group. Under these conditions, condensation reactions may occur to form hydroxo bridges. The bridging OH groups are noted as μ to distinguished them from terminal OH groups. This condensation process is known as olation (**eq. 1.2**).[11]

$$-\mathrm{M}-\mathrm{OH}+\ -\mathrm{M}-\mathrm{OH_2}\ \rightarrow\ -\mathrm{M}-\mathrm{OH}-\mathrm{M}-\ +\mathrm{H_2O} \qquad \mathbf{eq.1.2}$$

In the absence of an aquo ligand within the coordination sphere, hydroxo ligands may act as a leaving group.[11] The protons in the bridging OH ligands tend to be more acidic in a transition state during condensation. This grants proton transfer to another bridging OH ligand forming an H_2O ligand. This H_2O ligand may then act as a leaving group allowing condensation reactions to form oxo bridges. This process is known as oxolation.[11]

$$-\mathrm{M}\ -\mathrm{OH}+\ -\mathrm{M}\ -\mathrm{OH}\ \rightarrow \mathrm{M}-\mathrm{O}-\mathrm{M}+\mathrm{H_2O} \qquad \mathbf{eq.1.3}$$

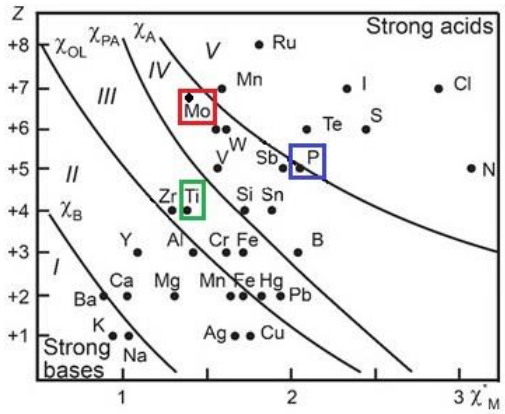

Figure 1.3 Electronegativities of metals (χM) vs. their cationic charges (Z), with contour lines that approximate their dominant condensation reaction types [Adapted from Ref. 11]

Therefore, for any type of condensation reaction, either oxolation or olation, to occur, the presence of hydroxo ligands in the coordination sphere is required. Which condensation reaction is dominant depends on the type of metal cation, type of ligands and the pH of the aqueous solutions. As depicted in **Figure 1.3**, cations that fall above the line χ_B (regions II, III, IV, and V) have a higher charge and electronegativity which would facilitate polarization of the oxide of the aquo ligand and the hydrolysis of it.[11,12] This leads to the unhindered proton transfer from the aquo ligand to a solvent water molecule, forming a hydroxo ligand which *may* subsequently undergo condensation. In region III, the condensation reactions can take place both by olation and by oxolation, between species such as $[Zr_4(OH)_{16}(OH_2)_8]^0$ or $[(TiO)_8(OH)_{12}]^{4+}$.[11] Region IV consists of strongly hydrolyzing metal cations such as V^{5+}, Mo^{6+} and W^{6+} that are of high charge and electronegativity.[11] The aquo ligands coordinated to these metal centers are unstable and become deprotonated to yield hydroxo ligands. Therefore, oxolation occurs in this region.

Cations that fall above the line χ_A (region V) behave as strong acids, without condensation. Likewise, the cations in the region II are stable in water but feature aquo ligands.[11]

By controlling these synthetic factors, researchers have been able to achieve a high degree of control over the composition and morphology of new compounds. Some of the beneficial properties of these modifications are high surface area, stabilized crystal structure and tunable novel surface properties.[11,12]

1.2 Aqueous Sol-Gel Chemistry of Titanium and Molybdenum with Peroxide

In our sol-gel synthesis of metal oxides with titanium, molybdenum and phosphate as building blocks, water-soluble peroxo complexes of these transition metals were employed as an alternative to alkoxide-based precursors, as the decomposition of the peroxo complexes are easily controllable in initiating the sol-gel reactions. Usage of hydrogen peroxide as a reactant includes many advantages such as, the reactant being a low impurity chemical, cost effectiveness, ease of removal from products and obtaining high purity compounds.

Aqueous chemistry of Ti^{4+} and Mo^{6+}, as well as their peroxo complexes, are described in this section. Mo^{6+} metal cations being smaller and highly charged relative to Ti^{4+} will interact strongly with aquo and/or hydroxo ligands.[8] The difference in ionic radius (Ti^{4+}: 0.76 pm; Mo^{6+}: 0.73 pm), charge, electronic configuration (Ti^{4+}: $3d^0$; Mo^{6+}: $4d^0$) and electronegativities of the metal cations can be used to understand their reactivity towards various solvents such as water and hydrogen peroxide.[8] While formation of sol particulates and gelation depend on the ionic size and charge of the metal cations, they may also be affected by the solvent, concentration, pH of the medium, drying/calcination temperatures.[8]

1.2.1 Aqueous Chemistry of Titanium

The Ti^{4+} metal cation in water tends to be unstable and instantly polymerize, to form precipitates or gel materials.[8] In water Ti^{4+} metal cations undergo hydrolysis and condensation to precipitate out TiO_2 particles, which limits the ability to explore new synthetic routes to produce Ti^{4+}metal ion based materials.[8]

In extremely low pH conditions, however, Ti^{4+} ions are found to be present in equilibrium, as Ti^{4+} ions coordinated to aqua ligands, $Ti(OH)_2^{2+}$ and TiO^{2+}.[13] A typical chemical compound used to prepare a Ti^{4+} precursor solution is titanyl sulfate dihydrate ($TiOSO_4 \cdot 2H_2O$).[14] The compound is available from Sigma-Aldrich in a technical grade of purity (≥29% Ti; ≤17% H_2SO_4).[15] As shown in **Figure 1.4**, the crystal structure of $TiOSO_4 \cdot 2H_2O$ contains two symmetry independent helices of corner-sharing TiO_6 octahedral units extending along the *a*-axis.[14] The helices are held together via corner-sharing tetrahedral SO_4 units. Two water molecules coordinate the Ti^{4+} ion to complete a TiO_6 octahedral unit. The H atoms in the aquo ligands are H-bonded to the oxygen atoms of two neighboring SO_4 units. Therefore, the helical chains are held together via H-bonding to form the three-dimensional structure.[14]

Lencka *et al*. have reported that, at pH < 2.45 the predominant species of Ti^{4+} is $Ti(OH)_2^{2+}$ when $TiOSO_4 \cdot 2H_2O$ is dissolved in water.[16] As shown in **eq. 1.4**, in highly acidic conditions the $Ti(OH)_2^{2+}$ would undergo oxolation reactions to form TiO_2 particles.[16]

$$Ti(OH)^{2+}_{2(aq)} \leftrightarrow TiO_{2(s)} + 2H^{+}_{(aq)} \qquad \textbf{eq. 1.4}$$

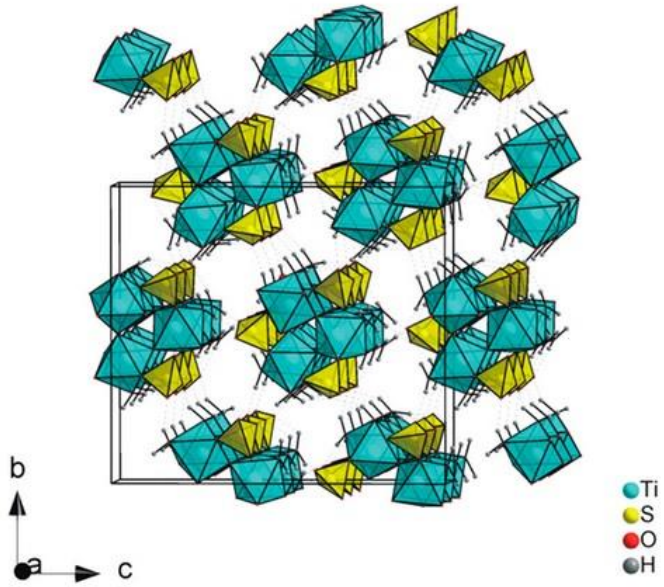

Figure 1.4 Structure of titanyl sulfate dihydrate [Adapted from Ref. 14]

The Ti^{4+} ions can be further stabilized by employing peroxide as a ligand, but the precise nature of the titanium-peroxide complexes is controversial. Besides, previous studies have been based on dilute aqueous solutions (1 – 5 mM) of titanium ions, while our synthesis employs much higher concentrations (~ 1 M).[17–20] A brief review is given on previous reports. It has been reported by Mori *et al*. that the reaction of hydrogen peroxide with a 1 mM Ti^{4+} solution, over the pH range of 0 – 13, can lead to four Ti^{4+} metal complexes stabilized by hydrogen peroxide ligands.[20] Below pH 2, the reaction produced an orange colored $[Ti(OH)_2(H_2O)(H_2O_2)]^{2+}$ species and at pH 3 – 6 yellow colored $[Ti(OH)_3(H_2O_2)]^{+}$ species was formed. At pH 7 – 9 a pale-yellow species $[Ti(OH)_3(O_2H)]^{0}$ was produced. While this species is unstable, having a large excess of hydrogen peroxide in reaction media can stabilize it and convert to a different species which has yet to be studied.[20] The presence of these species has been confirmed via absorption spectra data

and volumetric analysis studies (**eq. 1.5 – 1.8**). Finally, at pH > 10 a colorless species of $[Ti(OH)_2(O_2)_2]^{2-}$ was assumed to be formed. Further investigations are needed to determine the precise species.[20]

$$[Ti(OH)_2(H_2O)_2]^{2+}{}_{(aq)} + H_2O_{2(aq)} \leftrightarrow [Ti(OH)_2(H_2O)(H_2O_2)]^{2+}{}_{(aq)} + H_2O_{(l)} \quad (pH < 2) \quad \mathbf{eq.1.5}$$

$$[Ti(OH)_2(H_2O)(H_2O_2)]^{2+}{}_{(aq)} \rightarrow [Ti(OH)_3(H_2O_2)]^{+}{}_{(aq)} + H^{+}{}_{(aq)} \; (pH\ 3-6) \quad \mathbf{eq.1.6}$$

$$[Ti(OH)_3(H_2O_2)]^{+}{}_{(aq)} \rightarrow [Ti(OH)_3(O_2H)]^{0}{}_{(s)} + H^{+}{}_{(aq)} \quad (pH\ 8-9) \quad \mathbf{eq.1.7}$$

$$[Ti(OH)_3(O_2H)]^{0}{}_{(s)} + H_2O_{2(aq)} \rightarrow [Ti(OH)_2(O_2)_2]^{2-}{}_{(aq)} + H_2O_{(l)} + 2H^{+}{}_{(aq)} \quad (pH > 10) \quad \mathbf{eq.1.8}$$

Muhlebach *et al*. have reported the formation of peroxo-titanium species in a 1mM precursor solution, prepared by diluting a precursor solution mixture of 0.4 M $TiCl_4$ and 1.6 M hydrogen peroxide.[19] As shown in the following equation, the article describes the formation peroxo-titanium complexes in strongly acidic solutions;

$$Ti^{4+}_{(aq)} + H_2O_{2(aq)} \rightarrow [Ti(O_2)(OH)_{n-2}]^{4-n+}{}_{(aq)} + nH^{+}{}_{(aq)} \quad \mathbf{eq.1.9}$$

In **eq. 1.9**, *n* denotes the number of H^+ ions released when excess hydrogen peroxide is added to a Ti^{4+} precursor solution. However, the existence of $Ti(OH_2)_n^{4+}$ is doubtful, and does not occur above pH ~ 0. $TiCl_4$ readily hydrolyzes and undergoes condensation, in aqueous medium to form precipitates. This is precluded by lowering the pH of the medium. An acidic pH provided more control, over the hydrolysis and condensation rates of precipitation.[19] The article reports the presence of a mononuclear peroxo-titanium species $[Ti(O_2)OH]^+$ at pH ≤ 1 in a peroxo-titanium precursor solution, prepared using 1 mM $TiCl_4$ and 10 mM hydrogen peroxide solutions.[19] In the pH range of 1 – 3, addition of 0.1 M NaOH to the peroxo-titanium precursor solution led to the increase of pH of the medium. This facilitated the deprotonation of $[Ti(O_2)OH]^+$ to form species $[Ti_2(O_2)_2O(OH)]^+$ and $[Ti_2(O_2)_2O(OH)_2]$ as shown in the following equation[19];

$$2[Ti(O_2)OH]^+_{(aq)} \leftrightarrow [Ti_2(O_2)_2O(OH)^+]_{(aq)} \leftrightarrow [Ti_2(O_2)_2O(OH)_2]_{(s)} \qquad \textbf{eq. 1. 10}$$

When the pH of the peroxo-titanium precursor solution is at 3, the complex $TiO_2(OH)_2$ or its condensation product $[TiO_2O]_n{\cdot}H_2O$ were formed. At pH 7, a mononuclear peroxo-titanium species $[Ti(O_2)(OH)_3]^-$ was formed.[19] When the peroxo-titanium solution was titrated with NaOH, at pH 7 – 9, it produced anionic species $[Ti_2(O_2)_2O(OH)_3]^-$ and $[Ti_2(O_2)_2O(OH)_4]^{2-}$, by deprotonating water molecules coordinated to the metal atom of $[Ti_2(O_2)_2O(H_2O)_3]^{2+}$. The equilibrium reactions related to the deprotonation of $[Ti_2(O_2)_2O(H_2O)]^{2+}$ via OH^- is as follows[19];

$$[Ti_2(O_2)_2O(H_2O)_3]^{2+}_{(aq)} \leftrightarrow [Ti_2(O_2)_2O(OH)_3]^{-}_{(aq)}$$

$$\leftrightarrow [Ti_2(O_2)_2O(OH)_4]^{2-}_{(aq)} \quad \textbf{eq. 1.11}$$

The anionic species shown in **eq. 1.11**, eventually undergoes condensation to produce a precipitate of peroxo-titanium hydrate $TiO_2O{\cdot}H_2O$.[19]

Several studies have reported the use of hydrogen peroxide as a reactant to produce inorganic materials such as TiO_2, $H_2Ti_2O_5{\cdot}H_2O$, $(NH_4)_8[Ti_4(C_6H_4O_7)(O_2)_4]{\cdot}8H_2O$ and $Y_2Ti_2O_7$.[21–24] Jagadale *et al*. reported the synthesis of TiO_2 nanoparticles via peroxide-based sol-gel method.[21] Titanium tetra-isopropoxide ($Ti(OC_3H_7)_4$, 99.5%) was dissolved in ethanol and then hydrolyzed using water, to produce a white amorphous hydrous oxide precipitate. The precipitate, then, was reacted with H_2O_2 (30% w/v).[21] The precipitate dissolved to form a transparent orange sol of peroxo-titanium complex. With time the transparent orange sol underwent condensation to form a gel, which was later calcined to produce TiO_2 nanoparticles.[21]

Studies regarding synthesis of protonated layered titanate sheets produced at room temperature have been reported by Sutradhar *et al*.[22] An orthorhombic $H_2Ti_2O_5{\cdot}H_2O$ was synthesized using titanium-isopropoxide in an ammoniacal water-ethanol solution, aqueous ammonia carbonate and 30% hydrogen peroxide.[22]

Kakihana *et al*. have reported the synthesis of $(NH_4)_8[Ti_4(C_6H_4O_7)(O_2)_4]{\cdot}8H_2O$.[24] Typical synthesis involved dissolving Ti powder in a cold aqueous solution mixture of 30% hydrogen peroxide and 30% ammonia, to produce a yellow peroxo-titanium precursor.[24] Then to this peroxo-titanium solution, citric acid (CA) was added.[24]

Studies by Kumar *et al*. reported the synthesis of bulk and nanopyrochlore materials of composition $Y_{2-x}Ln_xTi_2O_7$ (Ln: Eu and Gd, x: 0.0 and 0.5) prepared using the sol-gel method with peroxo-titanium precursors.[23] A rare earth nitrate solution was mixed with a peroxo-titanium precursor solution which was prepared by adding titanium powder (100 mesh) to a mixture of 30% hydrogen peroxide, ammonia solution, citric acid (CA) and ethylene glycol (EG).[23] The final products obtained were identified as $Y_2Ti_2O_7$, $Y_{1.95}Eu_{0.05}Ti_2O_7$ and $Y_{1.95}Gd_{0.05}Ti_2O_7$.[23]

1.2.2 Aqueous Chemistry of Molybdenum

Mo^{6+} metal ion in inorganic compounds is important due to large electronegativity and propensity for reduction well as its role in providing a high Lewis acidity to the compounds. This has given rise to unique acid/base and redox properties.[25] These properties make molybdenum versatile for applications like catalysis, sensing and biomedicine.[25] Like Ti^{4+} ions, Mo^{6+} ions react with ligands such as water and hydrogen peroxide to form oxo-molybdenum (or "oxomolybdate") or peroxo-molybdenum species and undergo condensation.[12] These chemical processes are affected by solvent type, concentration, pH of the medium and drying/calcination temperatures.[12]

Haight *et al*. have reported that molybdenum species are generally stable as tetrahedral MoO_4^{2-} in pH > 6 (basic medium).[25] MoO_4^{2-} undergoes acid hydrolysis and condensation at pH 1 – 6, to form isopolymolybdates such as $Mo_7O_{24}^{6-}$ and $Mo_8O_{26}^{4-}$ (**eq. 1.12** and **1.13**).[26]

$$7MoO_{4(aq)}^{2-} + 8H^+_{(aq)} \rightarrow Mo_7O_{24(aq)}^{6-} + 4H_2O_{(l)} \qquad \textbf{eq. 1.12}$$

$$8MoO_{4(aq)}^{2-} + 12H^{+}{}_{(aq)} \rightarrow Mo_8O_{26(aq)}^{4-} + 6H_2O_{(l)} \qquad \textbf{eq. 1. 13}$$

Isopolymolybdates are compounds containing oxoanions with molybdenum in its highest oxidation state.[27] The larger polymeric extended structures of isopolymolybdates belong to group of compounds termed as polyoxometalates (POMs).[27] There are three main types of octa-molybdates, α-, β- and γ-$Mo_8O_{26}^{4-}$. The α and β forms of $Mo_8O_{26}^{4-}$ have been crystallized from solutions of Na_2MoO_4 in pH 3 – 4 by adding organic cations.[26]

Oyerinde *et al*. have reported the relationship between condensation reactions and pH of an acidic medium, using molybdate solutions of 0.1 and 10 mM concentrations.[28] At pH < 6, the condensation products had a greater dependence on molybdenum concentrations (**Figure 1.5**).[28] At molybdenum concentrations ≥ 10 mM and pH < 6, hexa-, hepta- and octa-molybdates are known to be the predominant species (**Figure 1.5**).[28] However, mononuclear species remained dominant at molybdenum concentrations no higher than 1 mM.[28]

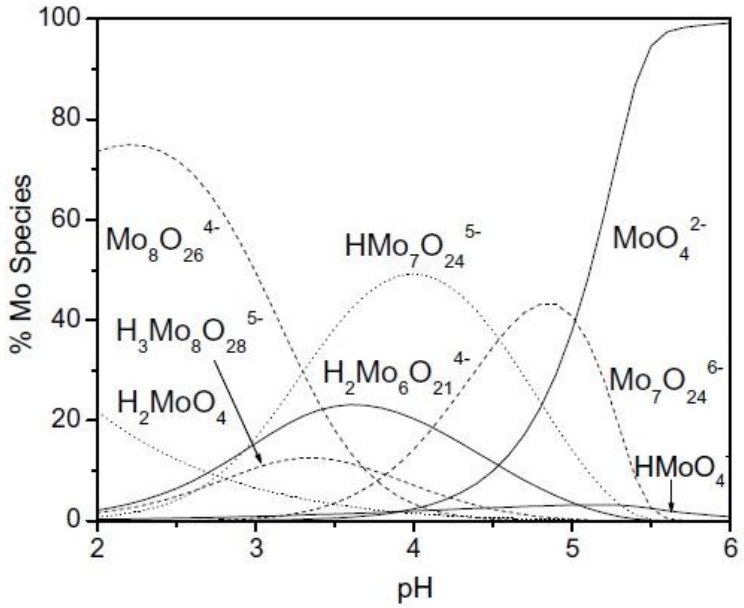

Figure 1.5 Mo speciation as a function of pH calculated from equilibrium constants at [Mo] = 10 mM [Adapted from Ref. 28]

Reactions between molybdate ions and hydrogen peroxide have been known. Csanyi *et al*. have reported, the presence of $[MoO_2(O_2)(OH)]^-$ ion in a solution mixture of 100 mM MoO_4^{2-} and 25 mM H_2O_2, at $[H_2O_2]/[MoO_4^{2-}] \leq 0.5$ and pH 7 (**eq. 1.14**). With a 100 mM H_2O_2 precursor solution at $[H_2O_2]/[MoO_4^{2-}] = 2$, however, the reaction in **eq. 1.15** would take place forming, $[MoO(O_2)_2(OH)]^-$.[29]

$$MoO_{4(aq)}^{2-} + H_2O_{2(aq)} \leftrightarrow MoO_2(O_2)(OH)^-_{(aq)} + OH^-_{(aq)} \qquad \textbf{eq. 1. 14}$$

$$MoO_{4(aq)}^{2-} + 2H_2O_{2(aq)} \leftrightarrow MoO(O_2)_2(OH)^-_{(aq)} + OH^-_{(aq)} + H_2O_{(l)} \qquad \textbf{eq. 1. 15}$$

In the presence of excess OH^- (100 mM MoO_4^{2-}; 25 mM H_2O_2), diperoxomolybdate ion, $MoO(O_2)_2(OH)^-$, would undergo dismutation by the OH^- to produce the tetraperoxomolybdate ion, $Mo(O_2)_4^{2-}$ as shown in **eq. 1.16**.[29]

$$2MoO(O_2)_2(OH)^-_{(aq)} + 2OH^-_{(aq)} \leftrightarrow Mo(O_2)^{2-}_{4(aq)} + MoO^{2-}_{4(aq)} + H_2O_{(l)} \quad \mathbf{eq.1.16}$$

In an acidic medium, Mo^{6+} ions are also present in the form of isopolymolybdates.[27,30] Some reported that peroxo derivatives of polymolybdates (polymolybdates: $Mo_7O_{24}^{6-}$, $HMo_7O_{24}^{5-}$, $H_2Mo_7O_{24}^{4-}$ and $Mo_8O_{26}^{4-}$) can be produced by adding small amounts of hydrogen peroxide, to a 4.40 mM MoO_4^{2-} solution in an acidic medium ($[H_2O_2/[Mo^{6+}] \leq 1.3$).[31] Species such as MoO_4^{2-}, $HMoO_4^-$, H_2MoO_4, $Mo_7O_{24}^{6-}$, $Mo_7O_{23}(OH)^{5-}$, $Mo_7O_{22}(OH)_2^{4-}$, $Mo_7O_{21}(OH)_3^{3-}$, $Mo_8O_{26}^{4-}$ and $Mo_{10}O_{34}^{8-}$ have been formed in various acidic solutions (pH 2 – 7) using a 10 mM MoO_4^{2-} precursor.[30] These species may undergo peroxidation to form various peroxo-molybdenum complexes as shown in **eq. 1.17** as an example. The acidic medium promotes the peroxidation of molybdate species but proton consumption may result in slight rise in pH of the solution mixture.[30]

$$Mo_7O^{6-}_{24(aq)} + 2H_2O_{2(aq)} \rightarrow Mo_7O_{22}(O_2)^{6-}_{2(aq)} + 2H_2O_{(l)} \quad \mathbf{eq.1.17}$$

In an acidic 10 mM MoO_4^{2-} precursor solution, the peroxidation of the dominant heptamolybdate species would gradually lead to smaller peroxo-molybdenum complexes, when the $[H_2O_2]/[Mo]$ mole ratio is increased to 6:1–14:1 (**eq. 1.18 – 1.20**).[30]

$$H_6[Mo_7O_{18}(O_2)_6]_{(aq)} + H_2O_{2(aq)} + H_2O_{(l)} \rightarrow H_8[Mo_5O_{15}(O_2)_4]_{(aq)} + H_2[Mo_2O_4(O_2)_3]_{(aq)} \quad \textbf{eq. 1. 18}$$

$$H_8[Mo_5O_{15}(O_2)_4]_{(aq)} + H_2O_{2(aq)} \rightarrow H_6[Mo_3O_{10}(O_2)_2]_{(aq)} + H_2[Mo_2O_4(O_2)_3]_{(aq)} \quad \textbf{eq. 1. 19}$$

$$H_6[Mo_3O_{10}(O_2)_2]_{(aq)} + H_2O_{2(aq)} \rightarrow H_2[Mo_2O_5(O_2)_2]_{(aq)} + H[MoO_2(O_2)(OH)]_{(aq)} \quad \textbf{eq. 1. 20}$$

It has been reported that by diluting the 10 mM precursor solution ($[H_2O_2]/[Mo] = 6 – 14$), diperoxomolybdic acid was obtained as a product.[30] As an example, for the sodium salt of heptamolybdate, the overall change in peroxidation is shown below (**eq. 1.21**),

$$6Na^+_{(aq)} + Mo_7O_{24}{}^{6-}_{(aq)} + 14H_2O_{2(aq)} \rightarrow 6Na^+_{(aq)} + [MoO(O_2)_2(OH)]^{6-}_{(aq)} + H[MoO(O_2)_2(OH)]_{(aq)} \quad \textbf{eq. 1. 21}$$

The acidic medium, however, protects the diperoxomolybdic species from undergoing further peroxidation, even with excess hydrogen peroxide.[30]

Krishnan *et al*. have reported the synthesis of MoO_3 using H_2O_2 as a reactant.[32] Molybdenum powder (99.99%) and 30% H_2O_2 were used to produce a 1.0 M peroxomolybdate precursor solution at pH 1.5.[32] The probable dissolution reaction of

molybdenum powder in 30% hydrogen peroxide, produced $H_2Mo_2O_3(O_2)_4(H_2O)_2$, as shown in **eq. 1.22**.[32] However, previous works by Kurusu *et al.* and by Segawa *et al.* suggested the formation of $MoO_2(OH)(O_2H)$ by dissolution of molybdenum powder in 30% H_2O_2 and subsequent evaporation of the peroxomolybdate solution (**eq. 1.23**).[32–34]

$$2Mo_{(s)} + 10H_2O_{2(aq)} \rightarrow H_2Mo_2O_3(O_2)_4(H_2O)_{2(aq)} + 7H_2O_{(l)} \quad \mathbf{eq.1.22}$$

$$Mo_{(s)} + 4H_2O_{2(l)} \rightarrow MoO_2(OH)(O_2H)_{(s)} + 3H_2O_{(l)} \quad \mathbf{eq.1.23}$$

As shown in **eq. 1.24** and **1.25**, the resulting species in peroxomolybdate precursor solutions $H_2Mo_2O_3(O_2)_4(H_2O)_2$ and $MoO_2(OH)(O_2H)$, eventually undergo disproportionation reactions to produce the final product MoO_3.[32]

$$H_2Mo_2O_3(O_2)_4(H_2O)_{2(aq)} \rightarrow 2MoO_{3(s)} + 3H_2O_{(l)} + 2O_{2(g)} \quad \mathbf{eq.1.24}$$

$$2MoO_2(OH)(O_2H)_{(s)} \rightarrow 2MoO_{3(s)} + H_2O_{(l)} + O_{2(g)} \quad \mathbf{eq.1.25}$$

1.2.3 Chemistry of polyoxomolybdates and polyoxotungstates

The chemistry of polyoxomolybdates and polyoxotungstates is one area this thesis work was inspired from. Therefore, it is summarized in this section.

Polyoxometalates are a category of metal oxides, mainly comprised of early transition metals (V, Nb, Ta, Mo, W) in their highest oxidation state. POMs were first synthesized by Berzelius in the early 19th century.[35] Most POMs are stable compounds,

that are soluble in water and behave as strong acids.[35] Due to its strong acidity and solubility in aqueous medium, POMs have been employed as homogeneous catalysts ($H_3PMo_{12}O_{40}$, $H_3PW_{12}O_{40}$, $H_4SiW_{12}O_{40}$), as an alternative to mineral acids (H_2SO_4, H_3PO_4).[35,36] As POMs undergo reduction reactions without decomposing or changing crystal structure, they have been deposited on substrates to be utilized as heterogeneous electrocatalysts ($H_6CoW_{12}O_{40}$).[35,37] Also, some POMs exhibit luminescent properties ($[\{Ce(dmf)_7\}_2(PMo_{12}O_{40})]$, $[\{Sm(dmf)_7\}_2(PMo_{12}O_{40})]$; dmf: dimethylfuran) and magnetic properties ($K_{12}[\{\beta\text{-}SiNi_2W_{10}O_{36}(OH)_2(H_2O)\}_2]\cdot 20H_2O$).[38,39] Medicinal properties that POMs ($K_6HPTi_2W_{10}O_{40}$, $K_7PTi_2W_{10}O_{40}$) exhibit are, anti-bacterial, anti-tumoral and anti-viral characteristics.[35,40,41]

Heteropoly acids (HPAs) are a group of solid acids, with the general formula $X_sM_nO_m^{y-}$ (M = metal atoms; Mo, W, V, Nb and Ta). It is a subcategory of POMs. HPAs consist of octahedral MO_6 units coordinated to tetrahedral oxoanionic units, with a central heteroatom X (X = P, As, Si and Ge).[35] HPAs (heteropoly-tungstates) were first discovered by Marignac in 1862.[35] Studies on HPAs are interesting due to unique traits like strong Bronsted acidity, redox, adsorption and ion-exchange properties, which stem from the diversification of charge, composition, size and structure.[35] Therefore, HPAs have the potential for a variety of applications, such as acid catalysts, redox catalysts, photocatalysts, electronic and protonic conductors, antitumoral and antiviral materials.[35] HPAs are characterized by the X/M ratio which defines the structure. One of the basic structures of HPAs is the Keggin (X/M = 1/12) structure.[35] The Keggin structure was first confirmed in 1933, where the structure of $H_3PW_{12}O_{40}$ was analyzed and discovered using X-ray crystallography.[35] In the Keggin structure, the heteroatom (X) is linked to four

oxygen atoms to form a tetrahedral unit XO_4 and each metal atom (M) is bonded to six oxygen atoms to form octahedral MO_6 units. The three, edge sharing octahedral units assemble to produce M_3O_{13} groups where they are connected (corner-sharing) to others and the M_3O_{13} octahedra groups are linked to the central heteroatom (**Figure 1.6**).[35]

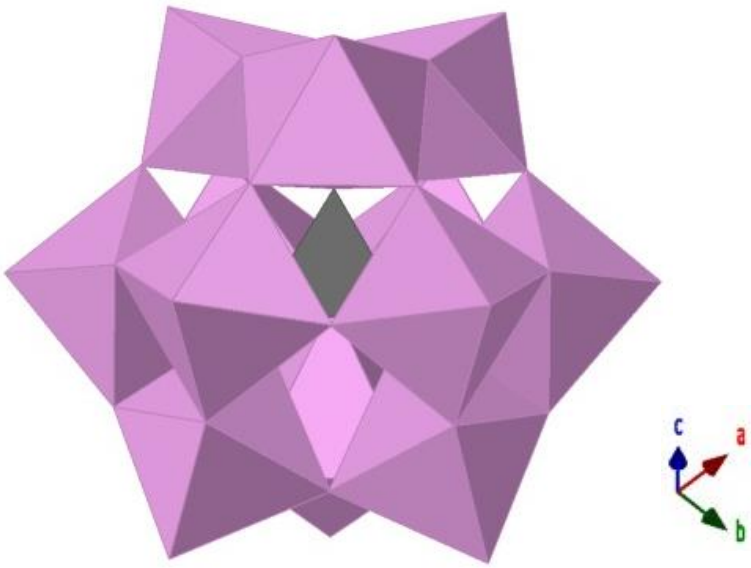

Figure 1.6 Keggin anion structure. The purple polyhedra represent the MO_6 octahedral units and the gray polyhedra represent the XO_4 tetrahedral unit [Adapted from Ref. 35]

The HPA, $H_3PMo_{12}O_{40}$ that has the Keggin structure is significant due to the similarities, in structural units (MoO_6 unit and PO_4 unit) and chemical properties (Bronsted and Lewis acidity) to that of $MoO_2(H_2O)(HPO_4)$, a crystalline compound synthesized in this study (described in Chapter 4).[35,42] One significant chemical property of HPAs, is the ability to undergo redox reactions without any structural change/destruction.[43] This redox property is highly favorable for electrocatalytic processes, particularly in the chemical sensing field. Chemical catalysis has been reported by Yang *et al.* as the use of phosphomolybdic acid ($H_3PMo_{12}O_{40}$) as a bifunctional catalyst for C—C bond formation

via the dehydrative reaction of diarylmethanols with different nucleophiles (2-naphthols, indoles, benzofuran and benzothiophene).[43] Compared to *p*-TsOH·H_2O (p-Toluenesulfonic acid monohydrate) the catalytic system produced an excellent yield, higher reaction rates and low catalyst loading when using the HPA catalyst. It is assumed that protons in $H_3PMo_{12}O_{40}$ might activate the alcohol, while the polyanion stabilizes the carbocation species.[43]

Unoura *et al*. reported that $[\alpha\text{-}SiMo_{12}O_{40}]^{4-}$ (**eq. 1.26**) and $[\alpha\text{-}PMo_{12}O_{40}]^{3-}$ (**eq. 1.27**) have been used as electrocatalysts for ClO_3^- ion reduction.[44] The third reduction wave of both HPAs represented conversion of species from the four electron reduced species to the six electron reduced species. This displayed the electrocatalytic ability of the HPAs, in the presence of ClO_3^- in 50% (v/v) dioxane water solution in 0.5 M H_2SO_4.[44] The ClO_3^- ion was reduced in the presence of H^+ ions to produce Cl^- ions and water, while regenerating the four electron reduced species. The electrocatalytic activity of 12-molybdophosphate was shown to be greater than 12-molybdosilicate (**eq. 1.26 and 1.27**).[44]

$$[H_4SiMo_{12}O_{40}]^{4-}{}_{(aq)} + 2e^- + 2H^+_{(aq)} \leftrightarrow [H_6SiMo_{12}O_{40}]^{4-}{}_{(aq)} \quad \mathbf{eq.1.26}$$

$$[H_4PMo_{12}O_{40}]^{4-}{}_{(aq)} + 2e^- + 2H^+_{(aq)} \leftrightarrow [H_6PMo_{12}O_{40}]^{4-}{}_{(aq)} \quad \mathbf{eq.1.27}$$

Most heteropoly acids are soluble in aqueous media which allows, pristine HPAs to be utilized in homogeneous acid catalyzed reactions due to their excellent solubilities in reaction media.[35] Protonated forms of HPAs can bear two acidic sites, acidic protons as the Bronsted acid sites and metal centers as the Lewis acid sites.[36] This makes HPAs act

as strong acids therefore, have been employed as acid catalysts in chemical reactions, instead of mineral acids (H_3PO_4 and H_2SO_4). It has been reported by Khozhevnikov *et al*. that $H_3PW_{12}O_{40}$ is stronger in acidity than $HClO_4$ and H_2SO_4.[36] The most common acid catalyzed reactions include hydration/dehydration, hydrolysis, esterification and transesterification.[36]

Da Silva *et al*. have reported the hydrolysis of macauba oil (vegetable oil), to free fatty acids using HPA catalyst $H_3PMo_{12}O_{40}$ compared to H_2SO_4.[45]

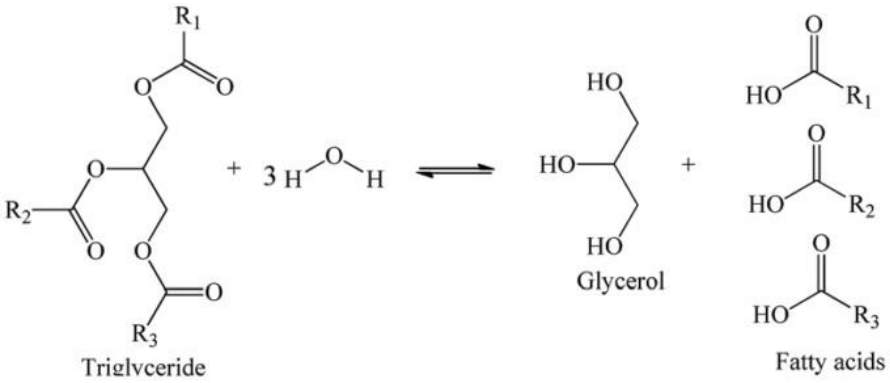

Figure 1.7 Hydrolysis reaction of triglyceride present in the vegetable oils [Adapted from Ref. 45]

The powdered form of $H_3PMo_{12}O_{40}$ was mixed in a sealed tube with vegetable oil and water.[45] The reaction mixture was heated to a temperature ranging 413 – 453 K for 8 hrs. After 8 hrs the mixture was cooled, and the contents were separated, to free fatty acids, glycerides, glycerol and water (**Figure 1.7**). The fatty acid yield was highest for $H_3PMo_{12}O_{40}$ at 39.4% while H_2SO_4 fatty acid yield was at 10.8%.[45]

One of the reported synthetic routes for $H_3PMo_{12}O_{40}\cdot 14H_2O$ is as follows, to 2.85 M aqueous solution of Na_2MoO_4, concentrated H_3PO_4 and concentrated HClO was added successively (**eq. 1.28**).[46,47] The disodium salt was precipitated from the yellow lukewarm solution. Then an aqueous solution of $Na_2HPMo_{12}O_{40}\cdot 14H_2O$ was acidified using

concentrated HCl, followed by addition of diethyl-ether for extraction.[46,47] Once the ether was removed by thermal decomposition at 100 °C, the concentrated aqueous solution of the heteropoly acid, underwent evaporation to produce yellow colored $H_3PMo_{12}O_{40}{\cdot}14H_2O$ crystals.[46,47] This method resulted in two disadvantages, low product yield and large amount of waste formation.[46,47]

$$12MoO_4{}^{2-}{}_{(aq)} + H_3PO_{4\ (aq)} + 21H^+{}_{(aq)} \rightarrow PMo_{12}O_{40}{}^{3-}{}_{(aq)} + 12H_2O_{(l)} \qquad \mathbf{eq.1.28}$$

Investigating an alternative sol-gel route to synthesize molybdenum metal phosphates with chemical properties like HPAs, would allow tuning of chemical properties (such as Bronsted and Lewis acidity), produce compounds with better crystallinity and higher yield. Also, added advantages such as low energy requirements, low-cost and lower waste production could be expected.

CHAPTER 2

CHARACTERIZATION METHODS

The following characterization methods have been used for analyzing the properties of synthesized materials: Powder X-ray diffraction (PXRD), Attenuated Total Reflectance-Fourier transform Infrared (ATR-FTIR) spectroscopy, Raman spectroscopy and scanning electron microscopy (SEM). Among these, PXRD and Raman spectroscopy were most extensively used for phase identification and structural analysis and are described in detail in this chapter.

2.1 Powder X-ray Diffraction (PXRD)

Powder X-ray diffraction is a widely used characterization technique due to several advantages such as its non-destructive nature, ease of sample preparation, high sensitivity, depth profiling and low maintenance cost.[48] When using PXRD for crystal structure determination, it provides a wide range of information such as unit cell parameters, lattice strain, tomographic distribution of defects and epitaxial layer thickness.[12,49]

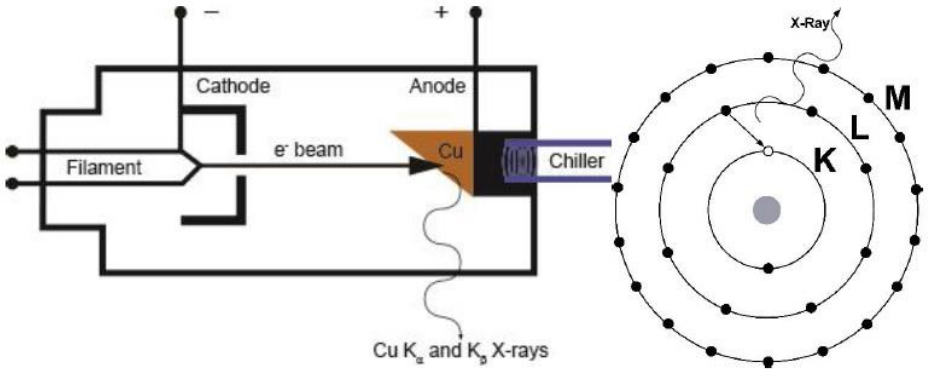

Figure 2.1 (left) Drawing of a cathode ray tube, (right) illustration of a vacancy in the K shell, and a Cu Kα transition that correlates to the emission of a characteristic X-ray [Adapted from Ref. 12]

Illustrated in **Figure 2.1** is a cathode ray tube that provides X-rays. A high-tension energy of 50 keV is applied to a Cu target to ionize its core electrons. When core electrons (K shell electrons) are ionized, the outer electron relaxes from the L to K shell, releasing Cu Kα X-rays at a wavelength of $\lambda = 1.5418$ Å.[12,49] The Kα component consists of two characteristic wavelengths assigned as $K\alpha_1$ and $K\alpha_2$ which correspond to transitions that occur from $2p_{1/2}$ to $1s_{1/2}$ and $2p_{3/2}$ to $1s_{1/2}$. Both Cu $K\alpha_1$ and Cu $K\alpha_2$ radiations are produced with characteristic wavelengths of $\lambda = 1.5406$ and Å; $\lambda = 1.5444$ Å. When a M shell electron relaxes to a vacancy in the K shell Cu K_β radiation with $\lambda = 1.392$ Å is emitted.[12,49] As X-rays have wavelengths on the same magnitude as atomic sizes and interatomic distances, X-rays travelling through a solid would diffract.[12,49] These X-rays are tuned using components such as slits, filters and diffractometers. For example, two of the most common filters used are Ni and Nb filters, which absorb the K_β radiation of target metals Cu and Mo.[12,49]

When considering detectors, gas flow detectors utilized to detect X-rays consist of, a gas mixture of 90% Ar and 10% methane gas which runs through a cathodic tube. X-rays (~ 15.7 eV per event) bombard Ar gas to ionize and produce ion pairs (positively charged ions and electrons).[12,49] High voltage is maintained between the cathode and anode to attract electrons to the anode and Ar^+ to the cathode, to produce an electrical current. The resulting number of electrical current pulses is proportional to the number of photons absorbed by the mixture of gases.[12,49] Another type of solid state detector used is Si (Li) detectors which utilize intrinsic Li-drifted Si single crystals. Interaction of X-ray photons with the detector generates electron-hole pairs, numbers proportional to the energy of the incident photon divided by the energy needed to generate a single pair.[12,49] Electrons and

holes respectively, travel to the cathode and anode producing a voltage dependent on the energy of the incident X-ray with an energy resolution of ~ 3.6 eV.[12,49]

As shown in **Figure 2.2** most PXRD diffractograms are collected using the Bragg-Brentano configuration.[12,49] In this configuration the divergent and diffracted beams are focused at a fixed radius from the sample position. Earlier diffractograms with poor intensity and peak width were obtained, due to the lack of focusing in flat plate diffractometers.[12,49] However, the modern flat plate diffractometer has good peak intensities and resolution due to better focusing of the diffracted beam.[12,49]

The Bragg-Brentano configuration consists of a cathode-ray tube that emits X-rays from a Cu target metal to produce an incident beam at an angle of elevation θ.[12,49] The diffracted beam is measured using a detector at an angle of elevation of θ, so the measurement takes place by scanning 2θ.[12,49]

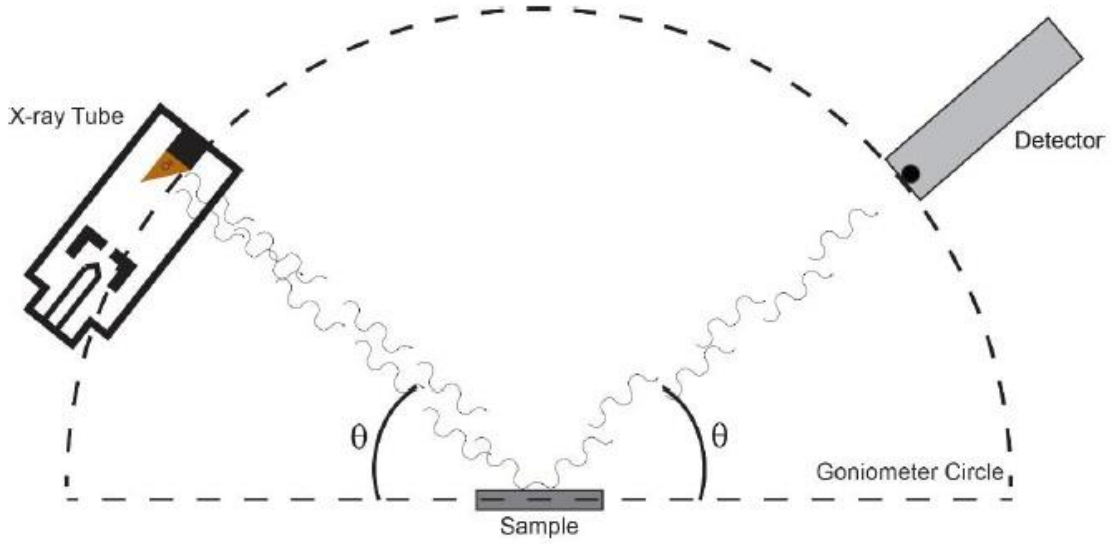

Figure 2.2 The Bragg-Brentano geometry for PXRD analysis [Adapted from Ref. 12]

When a sample is exposed to incident radiation, each electron in the sample compound interacts with the incident beam to produce a spherical elastically scattered wave as shown in **Figure 2.3**.[12,49] This scattering of X-rays creates identical scattered intensity in every direction. The intensity of coherently scattered X-rays is given by the Thompson equation (**eq. 2.1**).[12,49] In the Thompson equation I_0, I, θ, K and r, are termed as follows; the absolute intensity of the incident radiation, intensity of scattered wave, the scattering angle, constant (7.94×10^{-30} m^2) and distance between the electron and the detector.[12,49]

$$I = I_0 \frac{K}{r^2} \left(\frac{1 + \cos^2 2\theta}{2} \right) \qquad \textbf{eq. 2. 1}$$

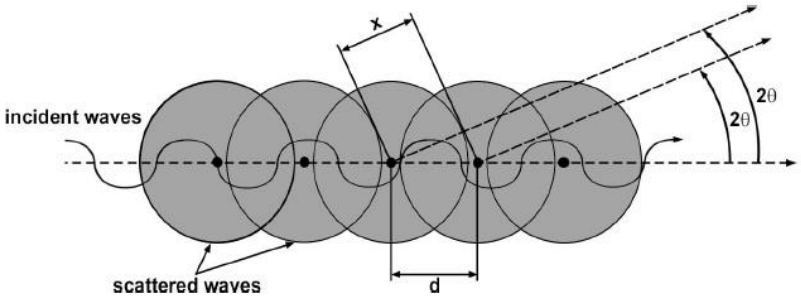

Figure 2.3 Diffraction from a line of scattering points irradiated along their axis of alignment [Adapted from Ref. 12]

As shown in **Figure 2.3**, 2θ is the angle at which the scattered waves will interact with each other constructively.[12,49] The phase difference between these waves is also called the phase angle (ϕ). At other angles the intensity of the signal would be negligible due to the destructive interference of out of phase scattered waves (**eq. 2.2**).[12,49]

$$\phi = 2\pi\left(\frac{d-x}{\lambda}\right) = 4\pi\left(\frac{d\sin^2\theta}{\lambda}\right) \qquad \textbf{eq. 2.2}$$

The phase angle, ϕ, describes the correlation between the intensity observed at a given angle of θ and the distance between the scattered waves.[12,49] With the three-dimensional arrangement of atoms in solids, the constructive interference may occur where the phase angle is intersected from all 3 dimensions. Therefore, when the incident wave is propagating along a vector that is not along the direction of the periodic spacing, the phase angle is described via the variable ψ (**Figure 2.4**). These correlations, between the directions of the incident and diffracted beams is given by the Laue equations (**eq. 2.3 – 2.5**).[12,49]

$$a(\cos\Psi_1 - \cos\phi_1) = h\lambda \qquad \textbf{eq. 2.3}$$

$$b(\cos\Psi_2 - \cos\phi_2) = k\lambda \qquad \textbf{eq. 2.4}$$

$$c(\cos\Psi_3 - \cos\phi_3) = l\lambda \qquad \textbf{eq. 2.5}$$

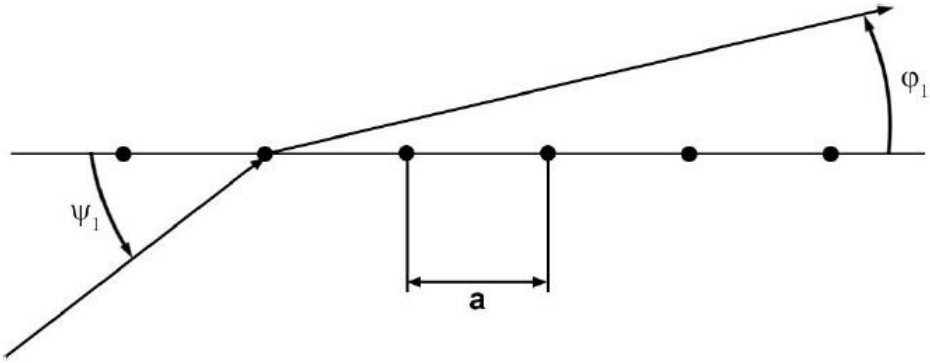

Figure 2.4 Diffraction from a line of scattering points irradiated from an angle ψ1 [Adapted from Ref. 12]

The Laue equations define conditions related to diffraction spots (Laue spots) visualized for single crystals, whereas powdered samples with crystallites, with random orientations would produce Laue rings in the reciprocal space.[12,49] These Laue rings formed in reciprocal space can be scanned in only one dimension as 2θ, to obtain crystal structure information. The Laue equations can be combined to Bragg's law (**eq. 2.7**).[12,49] Bragg's law describes the diffraction from crystallographic planes in crystalline samples as X-ray beams scatter from successive planes in the crystal structure (**Figure 2.5**). These scattered waves will travel distances differing by exactly one wavelength from each other (2Δ); which has easily been proven from the following diagram (**Figure 2.5**).[12,49] According to **eq. 2.6** the constructive interference is observed when,

$$2\Delta = n\lambda \qquad \textbf{eq. 2.6}$$

Where n is an integer and λ is the wavelength of the incident radiation.[12,49]

$$n\lambda = 2d\sin(\theta) \qquad \textbf{eq. 2.7}$$

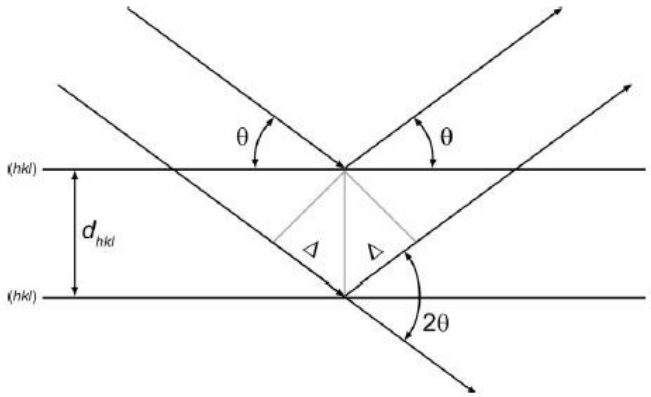

Figure 2.5 Illustration of Bragg's law for diffraction from crystal planes with index *hkl* in PXRD [Adapted from Ref. 12]

The Miller index of a Bragg peak (h, k, l) represents the order of the reflection along the a, b and c directions, respectively.[12,49] Each plane in a set (*hkl*) is periodic in the direction perpendicular to the planes and are equally spaced in the interplanar distance d_{hkl}. For a given set of Bragg peaks, the unit cell parameters can be refined.[12,49] For example, in the case of monoclinic crystal structure (**Figure 2.6**) with a low symmetry, the unit cell parameters *a*, *b*, *c*, α, β, and γ (**eq. 2.8**) can be determined by **eq. 2.9**, where V is the unit cell volume.[12,49] Unit cell parameters of a monoclinic crystal system is as follows,

$$a \neq b \neq c;\ \alpha = \gamma = 90°;\ \beta \neq 90° \qquad \textbf{eq. 2.8}$$

$$\frac{1}{d^2} = \frac{1}{V^2} = \frac{h^2}{(a^2 \sin^2\beta)} + \frac{k^2}{b^2} + \frac{l^2}{(c^2 \sin^2\beta)} + \frac{2\,hl\cos\beta}{(ac\,\sin^2\beta)} \qquad \textbf{eq. 2.9}$$

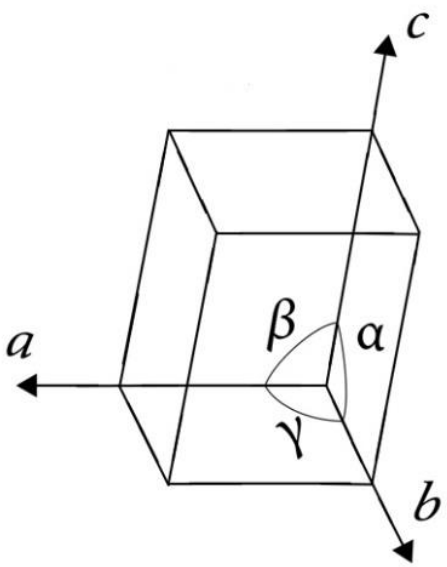

Figure 2.6 A monoclinic unit cell with unit cell parameters labeled [Adapted from Ref. 12]

Crystal structures with higher symmetries such as cubic, real space unit cell parameters are shown in **eq. 2.10**,

$$\frac{1}{d^2} = \frac{(h^2 + k^2 + l^2)}{a^2} \qquad \textbf{eq. 2. 10}$$

Using the Bragg's law, peak positions and relative intensities can be simulated.[12,49] The relative peak intensity is directly proportional to the structure factor ($|F_{hkl}|^2$) which is the absolute value of the square of the structure amplitude of the j^{th} atom at the fractional coordinates x, y and z (**eq. 2.11**). In **eq. 2.11**, n is the total number of atoms in the unit cell, g is the partial occupancy (often 1), *t(s)* is the thermal parameter, *f(s)* is the atomic scattering factor, and $s = \sin\theta_{hkl}/\lambda$.[12,49]

$$F_{hkl} = \Sigma_{j=1}^{n} g^j t^j(s) f^j(s) \exp[2\pi i(hx^j + ky^j + lz^j)] \qquad \textbf{eq. 2. 11}$$

The atomic scattering factor (f_j) of an atom (j) expresses how an electron cloud would scatter X-ray photons.[12,49] The atomic scattering factor increases as the atomic weight of the chemical species increases. Scattering events can be described using **eq. 2.12** with scattering parameters c_0, a_1–a_4 and b_1–b_4 and anomalous scattering parameters Δf_j' and Δf_j''.[12,49]

$$f^j = c_0^j + \exp \Sigma_{i=1}^{4} a_i^j \exp\left[-b_i^j \sin\frac{\theta}{\lambda}\right] + \Delta f^{j\prime} + i\Delta f^{j"} \qquad \textbf{eq. 2. 12}$$

Characteristic peak positions can be matched with databases to conduct phase identification for unknown crystal structures. In pure phase samples, Bragg peak positions would easily provide information related to unit cell parameters of the crystal structure. Peak broadness is interpreted as the nanoparticle size. It can be used to quantify the crystallinity of the sample.[12,49] Relative peak intensities of a PXRD pattern would be affected by certain aspects of the sample such as crystalline particle size, preferential orientation of the crystals and sample thickness. Instrumental effects such as background signal, the instrumental parameters including beam attenuators, collimators also would affect both peak positions and relative peak intensities.[12,49]

2.2 Raman Spectroscopy

The interest in Raman spectroscopy has vastly increased due to its many advantages. Raman spectroscopy is non-invasive and non-destructive.[50] It does not involve extensive

sample preparation and can easily be combined with other multivariate sample analyses methods. Structural information regarding individual chemical species and chemical compounds can easily be obtained using Raman spectroscopy due to its high spatial resolution. Another advantage that is offered through this technique is analyses of aqueous solutions and ability to monitor real time reactions, allowing studies in its natural environment.[50]

As opposed to absorption spectroscopy, Raman spectroscopy uses a monochromatic light source.[50] Most laser excited molecules at a virtual level, release the absorbed photons at the same frequency (ωo) giving rise to elastic or Rayleigh scattering. Fewer photons are re-emitted at wavelengths shifted, compared to the absorbed energy during excitation. This inelastic scattering is known as Raman scattering, where the amount of the difference in energy is exactly the difference between the initial state and the final energy level of the molecule.[50] Raman scattering has sub categorizes like anti-Stokes and Stokes scattering. The emitted photons of higher excitation energy than the absorbed light is known as blue shifted anti-Stokes scattering whereas, red shifted Stokes scattering is known to have a lower excitation energy than the incident light.[50] Typically, Stokes lines are stronger in intensity than anti-Stokes lines as the population of molecules at ground state is much larger than the population of molecules in the first excited state (**Figure 2.7**).[50,51] The quantum mechanical level description for Raman lines provide information on molecular properties that influence the intensity of Raman lines. The intensity of Stokes lines is given by **eq. 2.13**.[50]

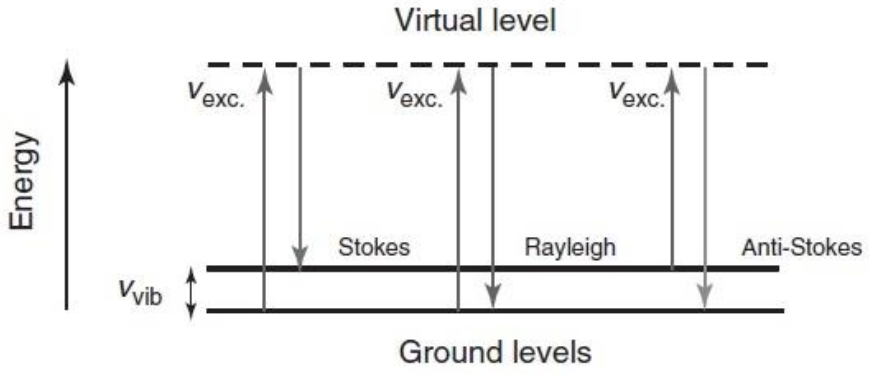

$$I_{Stokes} = \text{const. } I_0. \ (\omega_0 - \ \omega_R)^4. \ \left(\frac{\partial\alpha}{\partial q}\right)^2 \qquad \textbf{eq. 2.13}$$

Figure 2.7 Induced excitation states of molecules via Stokes, Rayleigh, or anti-Stokes excitation patterns [Adapted from Ref. 52]

I_o and ω_0 are the intensity and frequency of the incident light, ω_R is the frequency of the inelastically scattered light and ($\partial\alpha/\ \partial q$) is the change in the polarizability with respect to the change in the vibrational coordinate.[50,51] For a target molecule to be Raman active, the rate change of polarizability with the vibration must not be zero.[50,51]

The electromagnetic field (E) of the incident beam is characterized by its frequency (ω_0) and amplitude (E_0) (**eq. 2.14**).[50]

$$E = \ E_0. \cos \omega_0 t \qquad \textbf{eq. 2.14}$$

The electromagnetic field of the incident beam induces an electric dipole (μ) that leads to change in polarizability of the target molecule (α) (**eq. 2.15**).[50]

$$\mu_{ind} = \alpha E \qquad \textbf{eq. 2.15}$$

The induced dipole, when combined with the oscillating electromagnetic field, would oscillate with respect to the electromagnetic field (**eq. 2.16**).[50] Also, the target molecule would vibrate either in its ground state or excited state, due to contact with the electromagnetic field. The vibrating target molecule is expressed in **eq. 2.17**. In this equation ω_R is the resonance frequency of the vibrating molecule and q_0 the normal coordinate.[50]

$$\mu_{ind} = \alpha \cdot E_0 \cdot cos\omega_0 t \qquad \textbf{eq. 2.16}$$

$$q_t = q_0 \cdot \cos \omega_R t \qquad \textbf{eq. 2.17}$$

When the polarizability is expanded around q = 0 using the Taylor expansion (**eq. 2.18**),

$$\alpha = \alpha_0 + \left(\frac{\partial \alpha}{\partial q}\right)_{q=0} \cdot q \qquad \textbf{eq. 2.18}$$

The expression for polarizability can be rearranged as,

$$\mu_{ind} = \left[\alpha_0 + \left(\frac{\partial \alpha}{\partial q}\right)_{q=q0} \cdot q_0 \cdot \cos \omega_R t\right] \cdot E_0 \cdot cos\omega_0 t \qquad \textbf{eq. 2.19}$$

$$\mu_{ind} = \alpha \cdot E_0 \cdot cos\omega_0 t + \frac{1}{2}\left(\frac{\partial \alpha}{\partial q}\right)_{q=q0} \cdot q_0 \cdot E_0 \cdot \cos[(\omega_0 - \omega_R)t] + \frac{1}{2}\left(\frac{\partial \alpha}{\partial q}\right)_{q=q0} \cdot q_0 \cdot E_0 \cdot \cos[(\omega_0 + \omega_R)t] \quad \textbf{eq. 2.20}$$

In **eq. 2.20** the first term corresponds to Rayleigh scattering, while the second and third terms correspond to Stokes Raman scattering and anti-Stokes Raman scattering. Therefore **eq. 2.20** describes the distinct Raman band positions of target molecules.[50]

A basic Raman spectroscopic set-up consists of a monochromatic laser beam focused on a sample volume (**Figure 2.8**).[50] This enables precise excitation of the sample. Scattered light from the sample is collected by an optic angle and is focused by an imaging optic on to an entrance slit of the spectrograph. To obtain greater quality Raman scattering and to suppress unwanted Rayleigh scattering, a proper wavelength should be selected (**Figure 2.7**).[52] Near infra-red (NIR) lasers are preferred as they minimize fluorescence, because NIR lasers are of lower energy (longer wavelength) and is less likely to excite fluorescence. But a disadvantage of using NIR laser beams is that the available detectors become noisy.[52] Current FT-Raman spectroscopic instrument contains Nd/YAG lasers (1064 nm) that efficiently minimizes fluorescence and improve noise performance.[52] Early FT-Raman systems used flash lamp pumped versions of the Nd/YAG laser. Most systems now are equipped with diode-pumped versions that are effectively noise free. These offer optimum wavelength for fluorescence minimization and noise performance.[52]

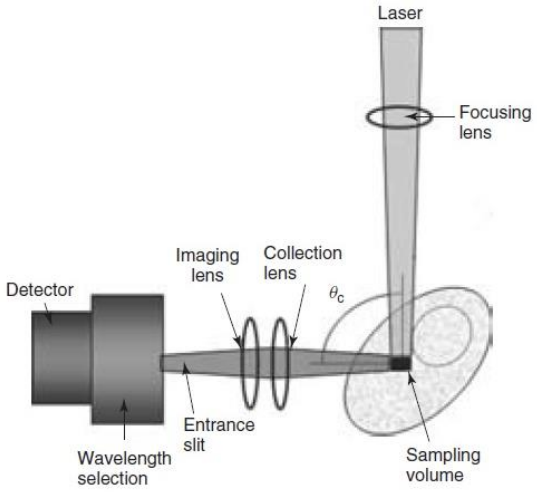

Figure 2.8 Sketch of an instrumentation set-up for Raman excitation of a sample. [Adapted from Ref. 52]

Collecting and filtering scattered radiation is an important aspect in Raman spectroscopy.[50,52] As Raman scattering is weak almost all scattered light arises from elastic scattering which provides no vibrational information. If allowed to pass through, it would completely saturate the detector. As the average Raman scattering efficiency is 10^{-8} a filter with an optical density (OD) of 8 at the laser wavelength will be used. The filter should minimally attenuate wavelengths longer than the laser wavelengths (inelastically scattered Raman photons) as Raman scattering intensities are low.[50,52] A saturated signal accompanied by noise could affect all frequencies of the Raman spectrum.[50,52] So, allowing extra Rayleigh scattering through filters would increase noise throughout the spectrum. Reduction of the Rayleigh line is obtained by using dielectric interference filters (DIFs), acoustic-optic tunable filters (AOTFs), birefringent filters (BFFs) and volume phase holographic filters.[50,52] These filters have better laser line attenuation with high

transmission which decreases the intensity of the Rayleigh line, below that of the strongest line in the spectrum.[50,52]

Another component of the FT-Raman spectrometer is the interferometer. Majority of focus is garnered towards optimization of the beamsplitter in the interferometer.[52] For NIR based analysis quartz or CaF_2 beamsplitters are preferred as they increase the modulation efficiency by 75%.[52]

Another important element in the spectrometer is detectors. Detectors allow coverage of both Stokes and anti-Stokes regions and minimizes the effect of background infrared radiation to the detector noise.[52] Germanium (Ge) and indium gallium arsenide (InGaAs) are two of the most prominently used detectors with detectivity approaching 1×10^{-15} W $Hz^{-1/2}$. Currently, the spectral bandwidth is optimal for both these detectors so further reductions in detector noise would not affect the sensitivity of the measurements.[52]

CHAPTER 3

NEW ACID MEDIUM SOL-GEL SYNTHESIS OF MIXED METAL PHOSPHATES, $Ti_{1-x}Mo_xP_2O_7$ (x = 0 – 0.5) AND $Mo_{1-y}Ti_yP_2O_{8-y}$ (y = 0 – 0.4)

3.1 **Introduction**

In recent years, tetravalent metal pyrophosphates (AP_2O_7, A = Ti, Sn, Zr, Ge, Si) have been of significant interest, due to their potential in many areas such as heavy metal absorbents ($Zr_{1-x}Ti_xP_2O_7$; x = 0, 0.2, 0.4, 0.5, 0.6, 0.8 and 1), proton conductors ($Sn_{0.95}Al_{0.05}H_{0.05}P_2O_7$), electrode material ($TiP_2O_7$), electrolytes ($TiP_2O_7$, SiP_2O_7) and catalysts (ZrP_2O_7, TiP_2O_7).[53–57] In particular, TiP_2O_7 has attracted considerable interest due to its potential in the above-mentioned fields as well as in areas like fuel cells, photocatalysis and anode material for aqueous lithium ion batteries.[57,58] TiP_2O_7 has advantages of chemical stability, ease of availability, low cost and its non-hazardous nature.[53–57] As this study mainly focuses on the synthesis of molybdenum-doped titanium pyrophosphate type compounds and *vice versa*, this introduction section will only include specifics pertaining to titanium and molybdenum pyrophosphates and their doped derivatives.

TiP_2O_7 has been synthesized in various ways including solid state, precipitation and sol-gel reactions. In a solid state synthesis, TiO_2 (particle size ~ 100 nm) was mixed with $(NH_4)_2HPO_4$ in a stoichiometric ratio and placed in a porcelain crucible followed by annealing the precursor mixture at high temperatures, 300 °C for 2 hrs and 800 °C for 10 hrs.[59]

Senguttuvan et al. reported synthesis of TiP_2O_7 through precipitation.[60] Titanium metal powder was dissolved in 85% H_3PO_4 and the suspension was heated at 170 °C for 1

hour, which yielded a dark blue solution. This solution was then continuously stirred for 24 hours.[60] Within the first 5 hours, a white precipitate evolved (**eq. 3.1**) and after 24 hours, formation of the white precipitate TiP_2O_7 came to completion.[60]

$$Ti_{(s)} + 2H_3PO_{4(aq)} + O_{2(g)} \rightarrow TiP_2O_{7(s)} + 3H_2O_{(l)} \qquad \mathbf{eq.3.1}$$

Shi *et al*. reported sol-gel synthesis of TiP_2O_7 utilizing block copolymer surfactants such as P123 ($HO(CH_2\text{-}CH_2O)_{20}(CH(CH_3)CH_2O)_{70}(CH_2CH_2O)_{20}H$).[61] P123 was ultrasonically dissolved in ethanol. Subsequently, $Ti(OC_4H_9)_4$ and 85% H_3PO_4 were added and stirred continuously for 10 hours at 40 °C (**eq. 3.2** and **3.3**).[12] The resulting sol solution was gelled in an open petri dish for 5 days at 30 °C. The gel was then dried at 130 °C for 5 days. The dried gel sample was calcined at 600 °C for 24 h to produce TiP_2O_7.[61]

$$Ti(OBu)_{4(l)} + 6H_2O_{(l)} \rightarrow Ti(OH_2)_2(OH)_{4(aq)} + 4BuOH_{(aq)} \qquad \mathbf{eq.3.2}$$

$$Ti(OH_2)_2(OH)_{4(aq)} + 2H_3PO_{4(aq)} \rightarrow TiP_2O_{7(s)} + 7H_2O_{(l)} \qquad \mathbf{eq.3.3}$$

The structure of TiP_2O_7 (a = 7.80(1) Å) was first described in 1935 by Levi *et al*.[62] The cubic crystal structure of TiP_2O_7 consists of TiO_6 octahedral and P_2O_7 dimeric tetrahedral units which share corners to form a three-dimensional network (**Figure 3.1**).[63] However, the crystal structure of TiP_2O_7 produced recently from solid state synthetic routes, was described as a superstructure (3a × 3a × 3a) with a cubic unit cell (space group: $Pa\bar{3}$) that included, corner-sharing TiO_6 octahedra and P_2O_7 dimeric tetrahedral groups in

a three-dimensional network.[64] Individual PO_4 tetrahedra (P–O bond distances: 1.5332 – 1.5815 Å) and TiO_6 octahedra (Ti–O bond distances: 1.82 – 2.00 Å) polyhedral units were distorted, with P–O–P bond angles of P_2O_7 units at 141.21(12)° – 144.51(13)°.[64] TiP_2O_7 synthesized under solid state conditions showed a lattice parameter of a = 23.6172 Å (volume = 13172.99 $Å^3$, density = 3.02 g cm^{-3}).[64] The crystal structure of TiP_2O_7 synthesized via the sol-gel method reported by Shi *et al*. was consistent with this, in that the compound had a superstructure (3a × 3a × 3a) with a cubic unit cell (space group: $Pa\bar{3}$) and a lattice parameter a = 23.6342 Å (volume = 13201.48 $Å^3$, density = 3.01 g cm^{-3}).[61,65]

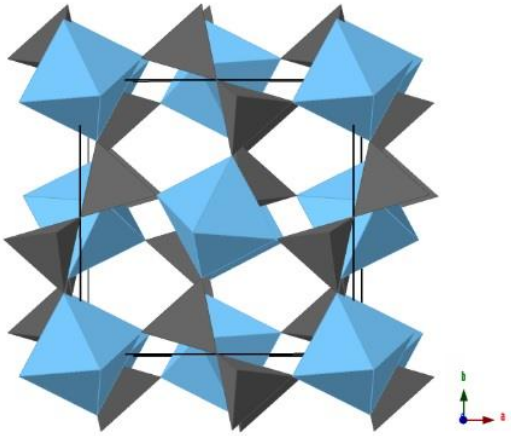

Figure 3.1 TiP_2O_7 crystal structure (along the *c*-axis) synthesized via the precipitation method. The blue colored polyhedral units represent octahedral TiO_6 units and the gray colored polyhedral units represent tetrahedral PO_4 units [Adapted from Ref. 60]

Interestingly, the precipitation method yielded TiP_2O_7 with the basic cubic unit cell (space group: $Pa\bar{3}$) with a lattice parameter of a = 7.9118 Å (volume = 495.261 $Å^3$, density = 2.962 g cm^{-3}).[60] The six Ti–O distances in the TiO_6 octahedra polyhedral unit were 1.93 Å which is slightly smaller than the expected value (1.96 Å) for a Ti^{4+} metal cation in an octahedral polyhedral unit, while the P–O–P angle of P_2O_7 units was 180°.[60]

In recent years doping titanium pyrophosphate with metal cations, has garnered attention due to the vast number of unique stable structural complexes and various synthesis processes it has given rise to. Doping pyrophosphate structures with high valent metal cations, has an improved effect on overall acidity, redox catalysis, conductivity, ion exchange and adsorption capacity in the crystal complex.[55,66]

Hibino *et al*. reported the synthesis of a hydroxide ion conducting antimony(V)-doped tin pyrophosphate electrolyte for alkaline fuel cells.[67] Partial substitution of Sn^{4+} cations by Sb^{5+}, led to OH^- ion exchange due to charge compensation for the high valent cations.[67] Sb^{5+}-doped tin pyrophosphates were produced via solid state synthesis. SnO_2 and P_2O_5 were mixed with H_3PO_4 and de-ionized water according to molar ratios of the desired product and stirred at 300 °C.[67] The highly viscous paste was calcined at 650 °C for 2.5 h to form a powder.[67] Among the synthesized solid crystal compounds $Sn_{0.92}Sb_{0.08}P_2O_7$ displayed the highest hydroxide ion conductivity 0.08 Scm^{-1} at 100.8 °C and 0.05 Scm^{-1} at 200.8 °C.[67] In this study, a significant improvement of electrical conductivity was shown for several other high valent metal ion doped SnP_2O_7 materials in the given order, $Sn_{0.92}Sb_{0.08}P_2O_7 > Sn_{0.92}Nb_{0.08}P_2O_7 > Sn_{0.92}V_{0.08}P_2O_7 > Sn_{0.92}Ta_{0.08}P_2O_7 > SnP_2O_7$.[67]

Synthesis of V^{5+}-doped TiP_2O_7 had been reported by Baker, where TiO_2 and a V_2O_5 were ground together and added to orthophosphoric acid in a porcelain crucible, with a Ti:V ratio ranging from 9:1 and 1:9, whilst maintaining a metal:P ratio of 1:6.[66] The solution was stirred at 150 °C for 3 hours until a melt was produced. Then the crucible was heated in an oven at 200 °C for 72 hours. The resulting paste was purified with de-ionized water and filtered.[66] Characterization studies conducted on the polycrystalline

products provided potential stoichiometries of V^{5+}-doped TiP_2O_7 as, $Ti_{0.853}V_{0.169}P_2O_7$, $Ti_{0.74}V_{0.16}P_2O_7$, $Ti_{0.849}V_{0.155}P_2O_7$, $Ti_{0.909}V_{0.117}P_2O_7$ and $Ti_{1.015}V_{0.081}P_2O_7$.[66] The report states that further studies need to be conducted to verify these compositions.[66] Other reported attempts of doping high valent metal cations to substitute Ti^{4+} cations in the TiP_2O_7 crystal structure, include Nb^{5+} and Ta^{5+}. However, the resulting final product series was amorphous.[68]

MoP_2O_8 was first reported in 1955 by *Schulz* but its crystal structure was described first in 1962 by *Kierkegaard*.[69] MoP_2O_8 was synthesized by adding a mixture of MoO_3 and P_2O_5 (1:4.4), into a platinum crucible, which was placed in an autoclave and heated at 500 °C temperature.[69] The purified crystals under the microscope, were reported to as small, thin and colorless flakes. While many other molybdenum phosphates have been synthesized and studied by multiple researchers for several decades, MoP_2O_8 has not been studied again since the report of *Kierkegaard*.[69] The crystal structure of the compound will be described in the later section where the XRD results are presented and discussed.

There have been, however, reports on synthesis of crystalline $(MoO_2)_2P_2O_7$ (Lister *et al.*) which has also been employed in Li^+/Na^+ ion intercalation reactions.[70–73] $(MoO_2)_2P_2O_7$ has been synthesized via the solid state route, using $MoO_2(H_2O)(HPO_4)$ as a precursor material. The solid precursor material was prepared by heating MoO_3 (99.95% metal basis) with H_3PO_4 in an autoclave at 180 °C for 12 hrs.[73] Next, the $MoO_2(H_2O)(HPO_4)$ precursor material was heated in an alumina crucible at 650 °C for 48 hrs, which resulted in crystalline $(MoO_2)_2P_2O_7$.[71,73]

The $(MoO_2)_2P_2O_7$ structure was first described by *Kierkegaard* in 1962 (**Figure 3.2**).[74] The crystal structure of $(MoO_2)_2P_2O_7$ can be described as follows, a crystal structure

with the space group *Pnma*, where Mo atoms are bound to O atoms to form MoO_6 octahedral units.[71,74] Every MoO_6 octahedral unit shares two Mo–O vertices with other MoO_6 octahedral units to form zigzag-chains along the *ac* plane.[71,74] Three of the four remaining vertices of MoO_6 octahedral units share its oxygen atoms with P_2O_7 dimeric tetrahedral units. All six vertices of P_2O_7 dimeric tetrahedral unit, are coordinated to MoO_6 octahedral units.[71,74]

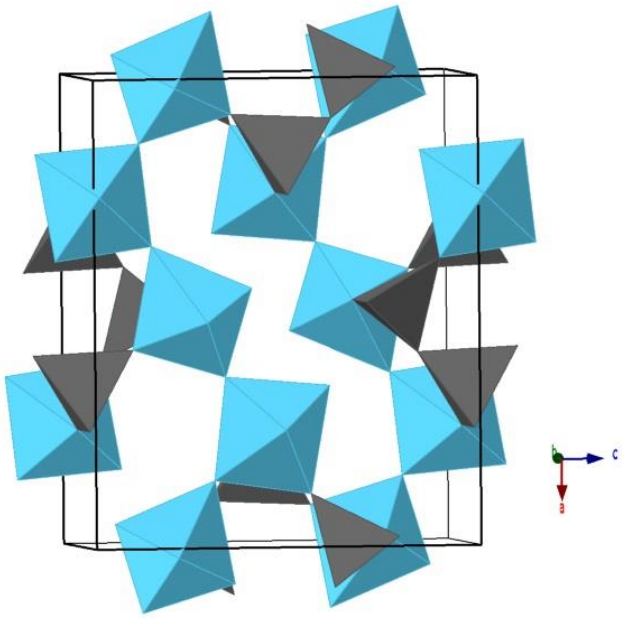

Figure 3.2 $(MoO_2)_2P_2O_7$ crystal structure (along the *ac*-plane) synthesized via solid state synthesis. The blue colored polyhedral units represent octahedral MoO_6 units and the gray colored polyhedral units represent tetrahedral PO_4 units [Adapted from Ref. 74]

In recent years $(MoO_2)_2P_2O_7$ has been intercalated with low valent metal cations like Li^+ and Na^+, to be used as a cathode material in lithium ion and sodium ion batteries.[70,75] $(MoO_2)_2P_2O_7$ has gained attention due to the ability, of the Mo metal center to undergo multielectron redox reactions.[70,75] Wen *et al*. reported that layered δ-$(MoO_2)_2P_2O_7$ was synthesized by heating the precursor $MoO_2(H_2O)(HPO_4)$ at 560 °C.[70] δ-$(MoO_2)_2P_2O_7$ underwent reversible intercalation of 1.2 lithium atoms per formula at 2.75

– 4.0 V voltage window (capacity: 70 mAh/g). After insertion of Li^+ ions in to the layered structure δ-$Li_{1.2}(MoO_2)_2P_2O_7$ was produced, where the oxidation state of the molybdenum metal center reduced from 6+ to 5.8+.[70]

Deng *et al*. reported intercalation of Na^+ ions in to the layered δ-$(MoO_2)_2P_2O_7$ structure.[75] Previously mentioned synthesis procedure had been followed to produce δ-$(MoO_2)_2P_2O_7$. Intercalation of 1.2 sodium atoms per formula, at 1.4 – 3.4 V voltage window (capacity: 70 mAh/g) was carried out to produce δ-$Na_{1.2}(MoO_2)_2P_2O_7$.[75]

Herein, this study focuses on exploring the synthetic versatilities of the acid medium sol-gel method, by replacing, Ti^{4+} metal cations with Mo^{4+} in the TiP_2O_7 crystal structure and Mo^{6+} metal cations by Ti^{4+} in the MoP_2O_8 crystal structure, where the metal to phosphorus ratio was fixed to be 1:2. Precursor solutions of both titanium and molybdenum were prepared by stabilizing Ti^{4+} and Mo^{6+} metal cations with hydrogen peroxide, to prevent immediate precipitation in aqueous medium. Hydrogen peroxide is an inexpensive, clean and non-hazardous reactant that offers the option for a much greener synthetic route compared to organic solvents. Phosphoric acid was used to acidify the reaction medium and to provide protons and phosphate ions as potential structural components. During the gelation process, lower heating temperatures were employed to allow better control of polycondensation reactions while calcination at 600 °C led to crystallization. Therefore, this new acid medium sol-gel synthetic method provides an energy and time efficient route to synthesize unique mixed metal phosphate materials.

When replacing Ti^{4+} cations by Mo^{4+} in the TiP_2O_7 crystal structure, the source of Mo^{4+} cations will be Mo^{6+} metal cations stabilized using hydrogen peroxide in a peroxo-molybdenum precursor solution. During the synthesis of $Ti_{1-x}Mo_xP_2O_7$ type

pyrophosphates, Mo^{6+} metal cations were to be reduced to Mo^{4+} leaving excess electrons in the d orbitals of the metal cation. In the synthesis of $Mo_{1-y}Ti_yP_2O_{8-y}$ type compounds, with the introduction of Ti^{4+} metal cations to the MoP_2O_8 crystal structure an oxygen deficiency was to be created to compensate the loss of Mo^{6+} cations in the structure.

3.2 Materials Synthesis

Samples were synthesized by adjusting synthetic parameters of titanium precursor solution volume, molybdenum precursor solution volume while keeping the phosphoric acid amount constant and were named systematically based on these variables (**Table 1** and **2**).

For a typical synthesis with the nominal P/(Ti+Mo) ratio of 2, an aqueous peroxo-titanium precursor solution was produced by dissolving 7.21 g of $TiOSO_4 \cdot 0.18H_2SO_4 \cdot 3.11H_2O$ (Sigma-Aldrich) in 3.78 g of 27 wt% H_2O_2 (Alfa Aesar) with magnetic stirring in an 80 mL glass jar, after which the stir-bar was removed. The nominal mole ratio of the peroxo-titanium precursor solution was H_2O_2/Ti was 1. An aqueous peroxo-molybdenum precursor solution was produced by gradually adding 2.88 g of molybdenum powder (1 – 5 μm, Aldrich) to 18.90 g of 27 wt% H_2O_2 (Alfa Aesar) with magnetic stirring in an 80 mL glass jar, submerged in an ice bath. Once all the molybdenum powder was added the stir-bar was removed. The nominal mole ratio of the peroxo-molybdenum precursor solution was (H_2O_2/Mo) was 5. Both precursor solutions were observed to be brick red in color.

To produce titanium molybdenum phosphate mixed metal compounds, the peroxo-titanium precursor solution and peroxo-molybdenum precursor solution were mixed together based on Ti/Mo mole ratios (1-x)/x; (x = 0 – 0.5) or y/(1-y); (y = 0 – 0.4), with

magnetic stirring in an 80 ml glass jar. A volume of 1.90 g of deionized water was added to the solution mixture and stirring was continued for 20 mins. Finally, a volume of 3.34 ml, 83.3 wt% H_3PO_4 solution in water (Alfa Aesar) was added to the mixture solution, while stirring for another 20 mins, after which the stir-bar was removed. The glass jar was covered with a lid and heated in a lab oven at 50 °C for 24 hrs. The cover was then removed, and the sample was heated further at 70 °C for 24 hrs to yield a yellowish orange sponge like wet gel. This resulting wet gel was calcined at 600 °C for 10 hrs in an ashing furnace (Carbolite, AAF1100) at a heating rate of 100 °C/hr, to produce solids which were homogeneous in color and texture all throughout the sample.

Table 1 Peroxo-titanium and peroxo-molybdenum precursor solution volumes for $Ti_{1-x}Mo_xP_2O_7$ (x = 0 – 0.5) samples

x	Volume of 2 M peroxo-titanium precursor solution (ml)	Volume of 2 M peroxo-molybdenum precursor solution (ml)
0	12.25	0.00
0.1	11.03	1.23
0.2	9.80	2.45
0.3	8.54	3.71
0.4	7.35	4.90
0.5	6.13	6.13

Table 2 Peroxo-titanium and peroxo-molybdenum precursor solution volumes for $Mo_{1-y}Ti_yP_2O_{8-y}$ (y = 0 – 0.4) samples

y	Volume of 2 M peroxo-titanium precursor solution (ml)	Volume of 2 M peroxo-molybdenum precursor solution (ml)
0.4	4.92	7.34
0.3	3.68	8.57
0.2	2.45	9.80
0.1	1.21	11.04
0	0.00	12.25

3.3 Materials Characterization

Powder X-ray diffraction (PXRD) patterns were obtained using Siemens D5000 diffractometer that consist of Cu Kα radiation. The ground samples were placed on a zero-background quartz sample holder and data were acquired by scanning 2θ from 10° to 90° with a step size of 0.0403° and a scan time of 30 min. The zero position of each PXRD pattern was first calibrated with a silicon powder internal standard (a = 5.4301 Å) and the background was subtracted. Reference PXRD patterns were searched and matched using the Find IT software and Crystal Diffract (Version 6.6.5). Crystal Maker (Version 10.0.5) was utilized to analyze and compare the resulting PXRD pattern with existing patterns and to draw the crystal structure.

3.4 Results and Discussion

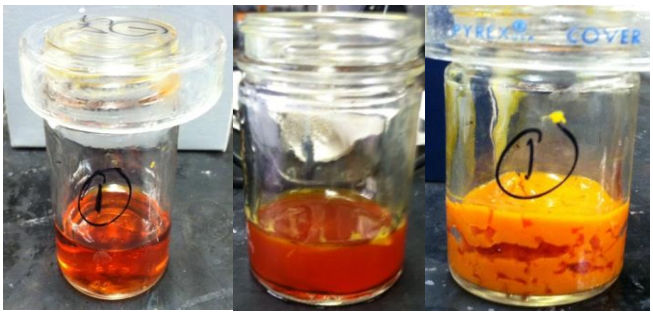

(a) (b) (c)

Figure 3.3 (a) Peroxo-titanium precursor solution (H_2O_2/Ti = 1), (b) Peroxo-molybdenum precursor solution (H_2O_2/Mo = 5), (c) Product after drying at 70 °C for 24 hrs

Figure 3.3 (a) and **(b)** are digital photographs of the peroxo-titanum and peroxo-molybdenum precursor solutions. The reddish orange color is characteristic of peroxo-titanium and peroxo-molybdenum complexes. The purpose of using peroxo ligands to stabilize metal cation complexes in their respective precursor solution was, to avoid the immediate precipitation of Ti^{4+} and Mo^{6+} metal cations with phosphate anions.[12] After the peroxo-titanium precursor and peroxo-molybdenum precursor solutions were mixed according to the Ti/Mo ratio, a volume 3.34 ml of 83.3 % phosphoric acid was added to the peroxo-metal ion mixed precursor solution. Subsequently, the peroxo-metal phosphoric acid mixture was dried at two different heating conditions which gave rise to a soft sponge-like wet gel with an orange color. The gel became lighter in color during heating (**Figure 3.3 (c)**), indicating the complexes were gradually losing the peroxo ligands. The yellow color of the wet gel indicates that a small amount of peroxo ligand still existed in the material.[12] The gel could be easily whipped into a wet paste.

It can be speculated that gelation was due to the reaction of the peroxo-titanium complex and peroxo-molybdenum complex with H_3PO_4. However, the exact reaction

mechanism and order of ligand exchange in the coordination sphere of the peroxo-metal complex is unclear. The highly acidic condition was chosen to avoid instant precipitation of Ti^{4+} and Mo^{6+} cationic complexes in their corresponding precursor solutions, as previously reported.[12] Although not described in detail here, an extremely high acidic condition was found to be less successful. With P/(Ti + Mo) = 3, gel products were obtained after drying (~24 hrs at 70 °C) and the final calcined products were not homogeneous in color and were amorphous. The top and bottom portions of the products were green in color, while the middle was brown or a mixture of green and brown components. Regardless of the colors, all the different parts of the product were amorphous. The final calcined product was hygroscopic, becoming a thick paste within a month by absorbing water. Further moisture absorption led to complete dissolution of the solid material within six months.

Figure 3.4 shows the PXRD patterns of the final products, with x varying from 0 – 0.5 for $Ti_{1-x}Mo_xP_2O_7$ type compounds (bottom – middle) calcined at 600 °C and y varying from 0.4 to 0 for $Mo_{y-1}Ti_yP_2O_{8-y}$ type compounds (middle – top) calcined at 600 °C, respectively. The Bragg reflection peaks for x = 0 of $Ti_{1-x}Mo_xP_2O_7$ correspond with the PXRD pattern of TiP_2O_7 synthesized via the precipitation method, where the crystal structure consisted of the basic cubic unit cell (space group: $Pa\bar{3}$) and a lattice parameter of a = 7.9118 Å.[60] After unit cell refinement studies were conducted on the TiP_2O_7 (x = 0) synthesized using peroxide based synthesis, it revealed that, the crystal structure consisted of a basic cubic unit cell (space group: $Pa\bar{3}$) and a lattice parameter of a = 7.8953(7) Å.[60] The PXRD patterns of x = 0.1 – 0.3 could be assigned to compounds with a single phase TiP_2O_7-type crystal structure.[60]

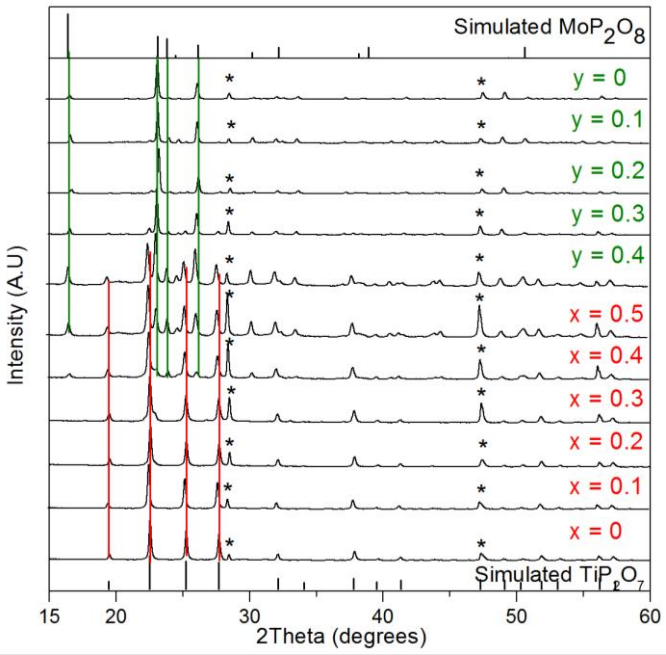

Figure 3.4 PXRD patterns of, simulated TiP_2O_7 crystal structure (bottom), final products calcined at 600 °C with nominal Ti:Mo = (1 – x)/x, x = 0 – 0.5 (bottom – middle), y/(1-y), y = 0 – 0.4 (middle – top) and simulated MoP_2O_8 crystal structure (top). Si (*a* = 5. 4301 Å) 28.445° and 47.300° reference peaks are represented by "*"

The Bragg reflection peaks of y = 0 of $Mo_{1-y}Ti_yP_2O_{8-y}$ matches that of the known crystal structure MoP_2O_8 while, the Bragg reflection peaks of y = 0.2 and 0.1 correspond to the MoP_2O_8-type structure.[69] Compared to the simulated PXRD pattern of MoP_2O_8, some of the relative peak intensities of the PXRD pattern of $Mo_{1-y}Ti_yP_2O_{8-y}$ (y = 0) showed differences. The relative intensity of peaks at 16.588° (110) and 23.946° (020) in the experimental PXRD patterns were lower compared to the simulated pattern, while the relative intensity of the peak at 23.133° (200) was higher. This observation is due to preferred orientation of the flat plate-like crystalline particulates during sample preparations. Preferred orientation can cause some Bragg planes to be more exposed to X-rays than others, resulting an increase of intensity in specific peaks.

For x = 0.4 and 0.5 of $Ti_{1-x}Mo_xP_2O_7$ and y = 0.3 and 0.4 of $Mo_{1-y}Ti_yP_2O_{8-y}$, the PXRD patterns indicate that the products were a mixture of two phases of the two different structure types. As shown in **Figure 3.4**, when x was increased from 0 to 0.5, peaks characteristic to TiP_2O_7 decreased in intensity and disappeared (**Figure 3.4** – red vertical lines), while when y was decreased from 0.4 to 0, peaks characteristic of MoP_2O_8 appeared with an increase in intensity (**Figure 3.4** – green vertical lines). All Bragg peaks in the mixed phase powder patterns can be assigned to TiP_2O_7 and MoP_2O_8.

All the final calcined products were homogeneous in color. The final calcined products where x = 0 of $Ti_{1-x}Mo_xP_2O_7$ was white in color whereas x = 0.1 – 0.4 were brown in color and x = 0.5 was green in color. The final calcined products where y = 0.4 of $Mo_{1-y}Ti_yP_2O_{8-y}$ was dark green in color and x = 0.3 – 0.1 were light brown in color. As shown in **Figure 3.5** the final calcined sample where y = 0 of MoP_2O_8 was of dark blue color.

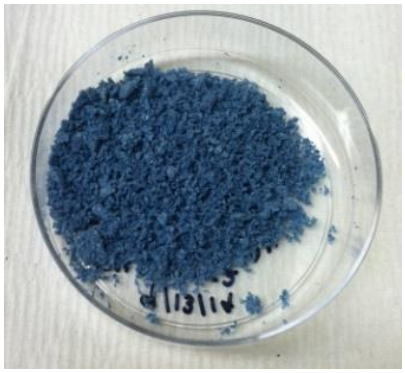

Figure 3.5 Final calcined sample MoP_2O_8; y = 0

The optical micrographs (**Figure 3.6**) of MoP_2O_8; y = 0 calcined sample shows transparent plate-like crystalline particulates of various shapes where some consists of sharp edges while others don't. The size of the particles ranges from 5 – 50 μm. Surface

morphology of the crystalline particulates are similar, and no special characteristics are visible.

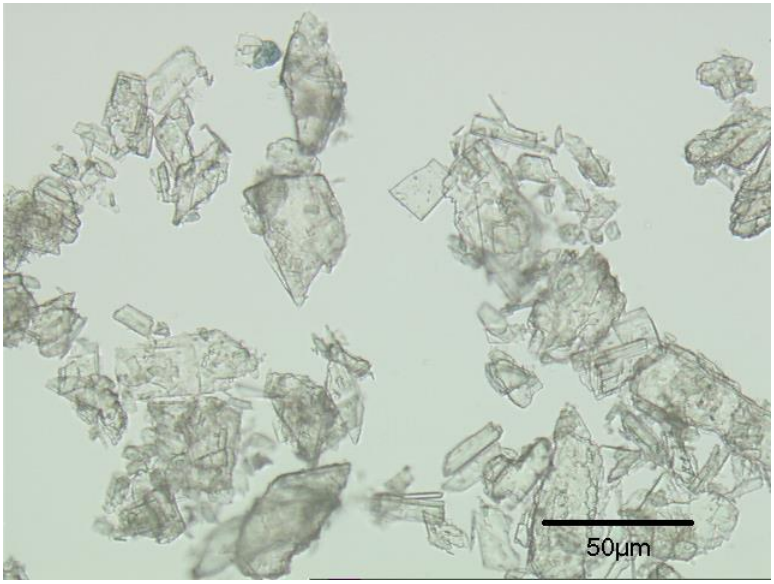

Figure 3.6 Optical microscopic image of final calcined sample MoP_2O_8 (y = 0)

The crystal structure of MoP_2O_8 (Space Group*: Pbcm*; *a* = 7.683 Å; *b* = 7.426 Å; *c* = 4.889 Å) was first reported by *Kierkegaard* in 1962.[69] MoP_2O_8 crystal structure consists of corner-sharing tetrahedral PO_4 units that form PO_3 chains which are parallel to the *c*-axis (**Figure 3.7**). The PO_3 chains consist of symmetrical tetrahedral PO_4 units with the following bonds, 2 × P–O_1; 1.583 Å, P–O_3; 1.553 Å and P–O_4; 1.528 Å. Molybdenum atoms are situated between PO_3 chains where each molybdenum atom is surrounded by six oxygen atoms which creates an octahedral environment.[69] In every octahedral arrangement, two oxygen atoms are bonded to a molybdenum atom with a bond distance of 1.773 Å. Two Mo–O_3 bonds of 2.227 Å and one Mo–O_4 bond of 2.006 Å create an asymmetrical MoO_6 octahedral unit. These asymmetric MoO_6 octahedral units then

assemble in a face sharing manner (**Figure 3.8**), resulting crystals built up of layers parallel to the *bc*-plane. It is worth noting that the layers are held together by van der Waal's forces.[69]

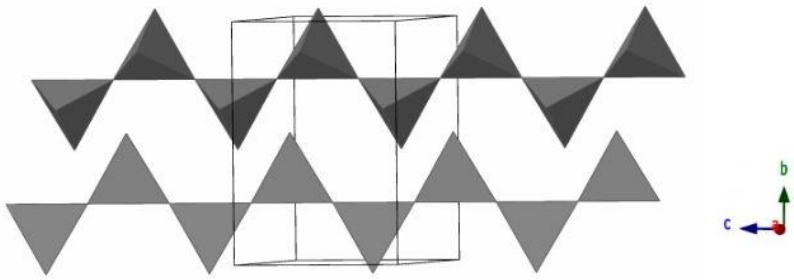

Figure 3.7 Two PO_3 chains viewed perpendicular to the *bc*-plane. The PO_4 tetrahedral polyhedral units are shown in gray [Adapted from Ref. 69]

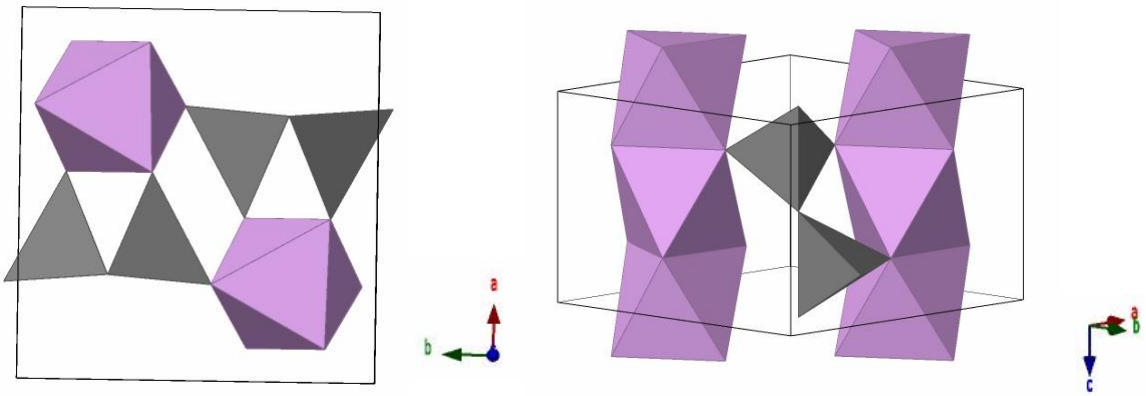

(a) (b)

Figure 3.8 (a) MoO_6 layers situated between two PO_3 chains viewed along the *ab*-plane, (b) Assembly of face shared MoO_6 octahedral units within the unit cell that forms layers along the *c*-axis. The PO_4 tetrahedral units are shown in gray and MoO_6 octahedral units are shown in purple [Adapted from Ref. 69]

3.5 Concluding Remarks

A new acid medium sol-gel synthetic route was developed to produce a series of $Ti_{1-x}Mo_xP_2O_7$ (x = 0 – 0.5) and $Mo_{1-y}Ti_yP_2O_{8-y}$ (y = 0.4 – 0) crystalline compounds. Also,

the synthesis of crystalline MoP_2O_8 (y = 0) was established via the above method. The new technique is distinctive, due to its use of hydrogen peroxide, to provide peroxo ligands to stabilize metal cations in its respective precursor solutions and to prevent immediate precipitation of metal cation complexes in aqueous medium. This method has shown to be time efficient and inexpensive compared to previously reported solid state and sol-gel synthetic routes. Having lower drying temperatures compared to the previous methods allowed better control over the condensation and crystallization of the final product. Therefore, the new method energy and time efficient when compared to previously reported synthetic routes.

Further investigations will need to be conducted to clarify the relationship between the precursor compositions and the unit cell parameters. Quantification of the amounts of Mo^{4+} and Ti^{4+} ion and the influence on chemical properties, such as Lewis acidity, need to be investigated as well as on the optical and electrical properties.

CHAPTER 4

PEROXIDE METHOD FOR SYNTHESIS OF $MoO_2(H_2O)(HPO_4)$

4.1 Introduction

Synthesis of $MoO_2(H_2O)(HPO_4)$ was first reported by *Schulz* in 1955.[73,76] The crystal structure of $MoO_2(H_2O)(HPO_4)$ was first described by *Kierkegaard* in 1958 as a structure (Space group $P2_1/m$, a = 6.7580 Å, b = 6.3390 Å, c = 7.0540 Å, β = 110.130°) that consist of alternating corner sharing octahedral MoO_6 units and tetrahedral PO_4 units (**Figure 4.1**).[76]

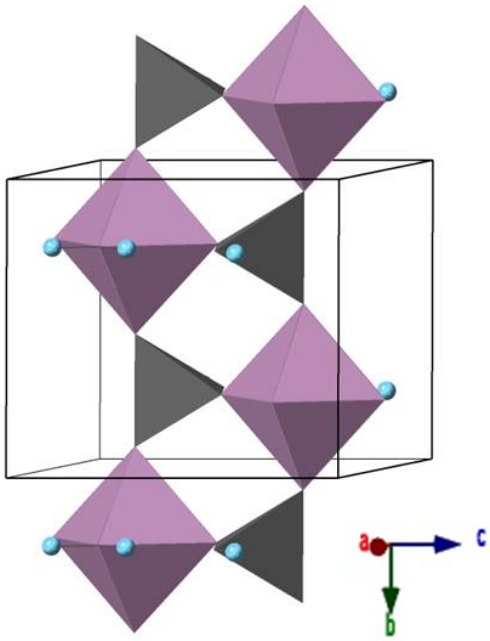

Figure 4.1 Double chain arrangement of MoO_6–PO_4 polyhedral units (along the *bc*-plane) in the $MoO_2(H_2O)(HPO_4)$ crystal structure. The purple colored polyhedral units represent octahedral MoO_6 units, the gray colored polyhedral units represent tetrahedral PO_4 units [Adapted from Ref. 76]

The asymmetrical octahedral MoO_6 unit consist of the following bonds, Mo–O_1; 1.682 Å, Mo–O_2; 1.723 Å, 2 × Mo–O_3; 1.998 Å, Mo–O_4; 2.108 Å, Mo–O_5; 2.267 Å. The

water molecule bound to the octahedral MoO_6 unit consists of two types of O–H bonds, O_5–H_2; 0.965 Å and O_5–H_3; 1.031 Å (**Figure 4.2**).[76] The symmetrical tetrahedral PO_4 unit entails four P–O bonds as such, 2 × P–O_3; 1.518 Å, P–O_4; 1.485 Å, P–O_6; 1.572 Å. A hydrogen atom is bound to the oxygen atom labeled O_6 of the PO_4 unit with a O_6–H_1 bond value 0.961 Å.[76] Every MoO_6 unit is bonded to three PO_4 units and every PO_4 unit is connected to three MoO_6 units building a double chain arrangement along the *bc*-plane.[76] The double chains are held together via hydrogen bonding created by the hydrogen atoms situated between the oxygen atoms (O_3–O_6) from different chains.[76]

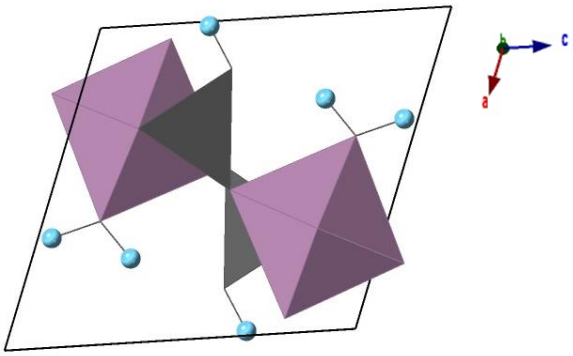

Figure 4.2 Water molecules attached to MoO_6 octahedral units and the H atom attached to PO_4 tetrahedral units (along the *ac*-plane) in the $MoO_2(H_2O)(HPO_4)$ crystal structure. The purple colored polyhedral units represent octahedral MoO_6 units, the gray colored polyhedral units represent octahedral MoO_6 units, the gray colored polyhedral units represent tetrahedral PO_4 units and the blue spheres represent H atoms [Adapted from Ref. 76]

Lister *et al*. have reported the dehydration mechanism of $MoO_2(H_2O)(HPO_4)$.[73] On heating to 150 °C, a new poorly crystalline β-$MoOPO_4$ and an amorphous material were formed.[73] Further heating above 427 °C produced an intermediate phase δ-$(MoO_2)_2P_2O_7$ and above 500 °C the fully dehydrated γ-$(MoO_2)_2P_2O_7$ was formed.[73]

Compared to the synthetic route reported by *Schulz*, the new peroxide-based synthesis method reported in this study used hydrogen peroxide as a stabilizing ligand in a peroxo-molybdenum precursor solution, in the presence of phosphate ions and strong acidic medium.[73,76] Gradual decomposition of the formed peroxo-molybdenum phosphate complex was possible upon a gentle heating, which enabled slow and controlled synthesis of crystalline $MoO_2(HPO_4)(H_2O)$ with 70 % yield. This peroxide-based synthesis method didn't involve any organic reactants and has a simple experimental procedure. As the only solvents used in the synthesis were hydrogen peroxide and water, the synthetic route is of low cost and non-hazardous conditions.

4.2 Materials Synthesis

The concentration of the peroxo-molybdenum precursor solution was 2.0 mol/L and Mo/P ratio was 1. For synthesis of samples with the nominal H_2O_2/Mo ratio 6.5, an aqueous solution of peroxo-molybdenum precursor was produced by dissolving 5.76 g of molybdenum powder (1 – 2 μm, ≥ 99.9% trace metal basis, Sigma Aldrich) in 49.13 g of 27 wt% H_2O_2 (Alfa Aesar) with magnetic stirring in a 250 mL glass beaker (placed in an ice bath), after which the stir-bar was removed. Once the peroxo-molybdenum precursor solution had cooled off, 24.50 ml of peroxo-molybdenum precursor solution was added to 7.15 g of deionized water in an 80 ml glass jar. After stirring the mixture for 20 mins, 3.40 ml of 83.3 wt% H_3PO_4 solution in water (Alfa Aesar) was added and stirred for another 20 min. The glass jar was covered with a glass petri dish and dried in a lab oven at 70 °C for 72 hrs. Then the partially covered sample was dried further at the same temperature for 72

hrs which resulted in a white solid. Finally the solid was rinsed with anhydrous acetone for purification.

4.3 Materials Characterization

Powder X-ray diffraction (PXRD) patterns were obtained using a Siemens D5000 diffractometer with Cu Kα radiation. The ground sample was placed on a zero-background quartz sample holder and data was obtained by scanning 2Theta from 10° to 90°with a step size of 0.0403° and a scan time of 30 min. The zero position of each PXRD pattern was first calibrated with a silicon powder internal standard (a = 5.4301 Å) and the background was subtracted. Reference PXRD patterns were searched and matched using the Find IT software and Crystal Diffract (Version 6.6.5) and Crystal Maker (Version 10.0.5) were utilized to analyze and compare the resulting PXRD pattern with existing patterns and to draw the crystal structure. Unit cell parameters were determined by using the HighScore Plus X'Pert Pro software (Version 2.2c (2.2.3)). Scanning electron microscopy (SEM) studies were performed using a FEI XL-30 Environmental SEM using 5 and 15 keV electrons respectively on dry-ground samples. Raman and ATR-FTIR spectra were obtained on a Bruker IFS66V/S spectrophotometer.

4.4 Results and Discussion

$MoO_2(HPO_4)(H_2O)$ was first reported by *Schulz* in 1955.[73,76] The compound was synthesized by first dissolving MoO_3 (15 g) in a concentrated H_3PO_4 solution (14.5 M) at 180 °C.[76] After the solution cooled down crystallization of the compound occurred when an excess amount of a concentrated HNO_3 (15.5 M) was added to the solution and

subsequently the solution was heated to gradually evaporate water. The crystals were filtered off rinsed with cold water and air dried.[76]

In this peroxide-based synthesis 83.3 wt% H_3PO_4 solution (Alfa Aesar) was added to the peroxo-molybdenum precursor solution (H_2O_2/Mo = 6.5) where P/Mo = 1. Consequent drying of the precursor mixture led to the final product a white solid shown in **Figure 4.3**. It is notable stating that along with the H_2O_2/Mo = 6.5 peroxo-molybdenum precursor solution two other H_2O_2/Mo ratios 5 and 7.5 were explored during the experiment to decipher the accurate nominal H_2O_2/Mo ratio that would lead to a homogeneous crystalline product.

Figure 4.3 Final product synthesized with H_2O_2/Mo = 6.5

The new peroxide-based synthesis method reported in this study used peroxo-molybdenum precursor solutions with lower concentrations (2.0 mol/L) which were prepared using molybdenum powder and 27 wt% H_2O_2.[73,76] The peroxide ligands coordinated to the metal cation, prevented the metal cations from readily precipitating in aqueous medium. The low amount (less than 5 ml) of H_3PO_4 added to the peroxo-molybdenum precursor solution acted as a proton provider to the crystal structure of the

final product. The final precursor mixture was dried at a lower temperature (70 °C) compared to the method reported by *Schulz* .[73,76]

Hence, the novel method allowed atomic level mixing of precursors, lower reaction temperatures and noncorrosive reaction conditions which led to an energy efficient synthesis.

Figure 4.4 Peroxo-molybdenum precursor solution H_2O_2/Mo = 6.5

Figure 4.4 is a representative photograph of the aqueous peroxo-molybdenum precursor solution with nominal H_2O_2/Mo= 6.5 showing the characteristic red color. The precursor solution in a closed container at room temperature remains a red colored solution for approximately 10 hrs. This affirms the stability of the peroxo-ligands present in the precursor solution. The peroxo-molybdenum precursor solution was further analyzed using Raman spectroscopy.

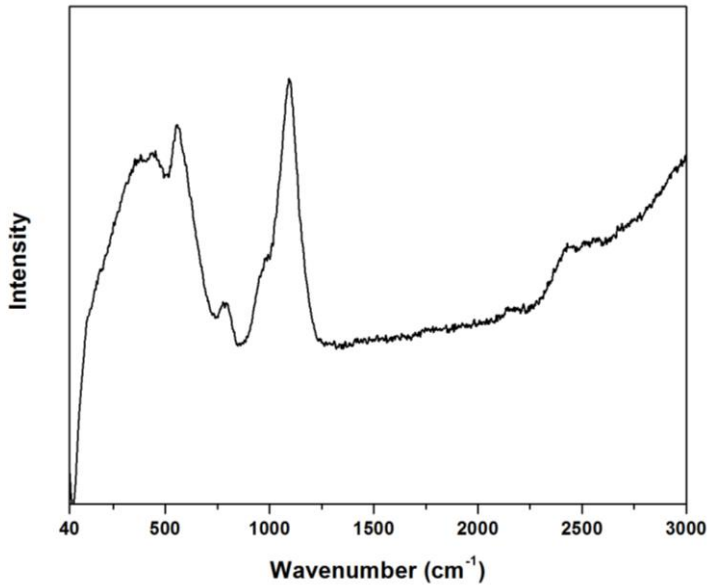

Figure 4.5 Raman spectrum of peroxo-molybdenum precursor solution; H_2O_2/Mo = 6.5

Figure 4.5 shows the Raman spectrum from 40 to 3000 cm^{-1} of a peroxo-molybdenum precursor solution (50 mM) that was prepared at H_2O_2/Mo = 6.5. The peak between 300 – 400 cm^{-1} in the spectrum correspond to bending vibrations of O–Mo=O bonds.[29,77–84] Whereas, peaks between 600 – 700 cm^{-1} and 1000 – 1100 cm^{-1} can be assigned to stretching vibrations of Mo–O bonds.[29,77–84]

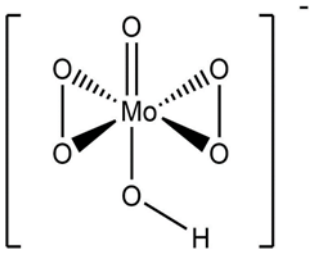

Figure 4.6 $[MoO(O_2)_2OH]^-$ structure [Adapted from Ref. 29]

Further analysis revealed that the peak at 400 cm^{-1} could be assigned to asymmetric stretching vibration of $Mo(O_2)$ and peaks at 1000 cm^{-1} and between 700 – 800 cm^{-1} correspond to vibrational modes of O–O bonds.[77–82,85,86] While this analysis explains the presence of Mo–O bonds, Mo=O bonds and O–O bonds closer observation of the Raman spectrum shows a broad peak at 1750 cm^{-1} corresponding to bending vibrations of H_2O_2. The peaks near 1750 cm^{-1} can, also be ascribed to bending vibrations of H_2O whereas, 2180 cm^{-1} and peaks between 2450 – 2600 cm^{-1} can be assigned to stretching vibrations of H_2O.[77–82,85,86] These bonding arrangements may be assigned to $[MoO(O_2)_2OH]^-$ structure (**Figure 4.6**) but further studies will need to be conducted to verify the species present in the peroxo-molybdenum precursor solution.[29,77–84]

Figure 4.7 shows the PXRD patterns of the final products with H_2O_2/Mo = 5, 6.5 and 7.5. The PXRD patterns of samples with H_2O_2/Mo = 5 and 7.5, show patterns with broad peaks that indicate the presence of an amorphous phase as a major component and a few sharp peaks that indicate a small amount of crystalline phase. The PXRD pattern of H_2O_2/Mo = 6.5 is crystalline and all Bragg peaks match the PXRD pattern of the crystalline compound $MoO_2(H_2O)(HPO_4)$. Based on the composition of the final product with H_2O_2/Mo = 6.5 the synthesis could be due to the reaction between $[MoO(O_2)_2OH]^-$ and H_3PO_4 as follows (**eq. 4.1**):

$$[MoO(O_2)_2OH]^-_{(aq)} + 2H_3PO_{4(aq)}$$

$$\rightarrow MoO_2(H_2O)(HPO_4)_{(s)} + [H_2PO_4]^-_{(aq)} + H_2O_{(l)} + O_{2(g)} \quad \mathbf{eq.4.1}$$

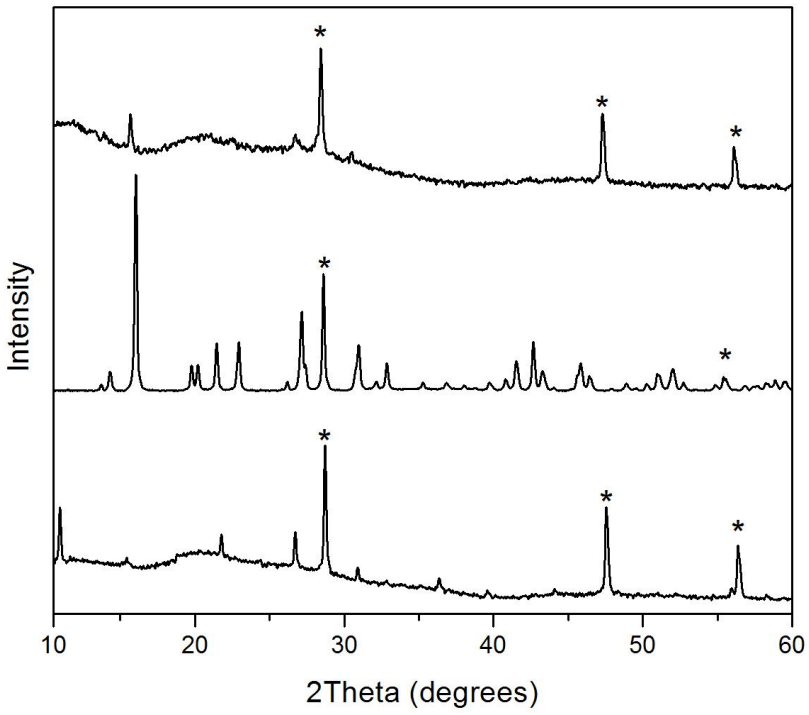

Figure 4.7 PXRD patterns of final purified products of H_2O_2/Mo = 5 (bottom), 6.5 (middle) and 7.5 (top). The Bragg peaks of Si (*a* = 5.4301 Å) are represented by '*'

The final purified product was imaged using the optical microscope and SEM to study its morphology. The optical micrographs (**Figure 4.8**) show transparent crystalline particulates with dimensions ranging from 20 to 100 µm. The crystalline particulates have various shapes, some with sharp edges.

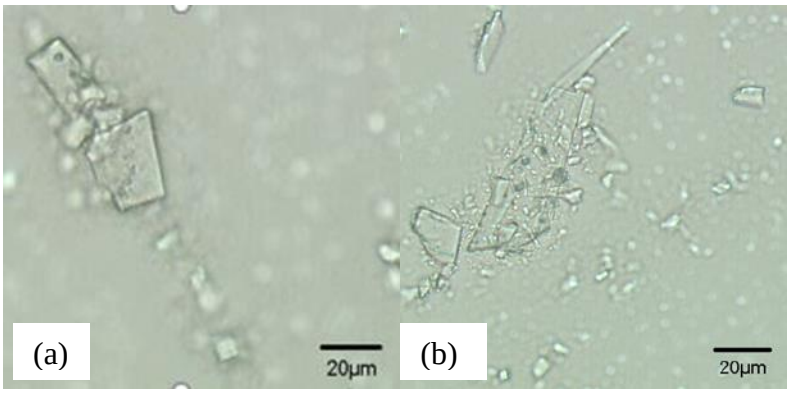

Figure 4.8 Optical micrographs of (a) and (b) solid samples synthesized with H_2O_2/Mo = 6.5 and P/Mo = 1. Scale bars are 20 µm for both (a) and (b)

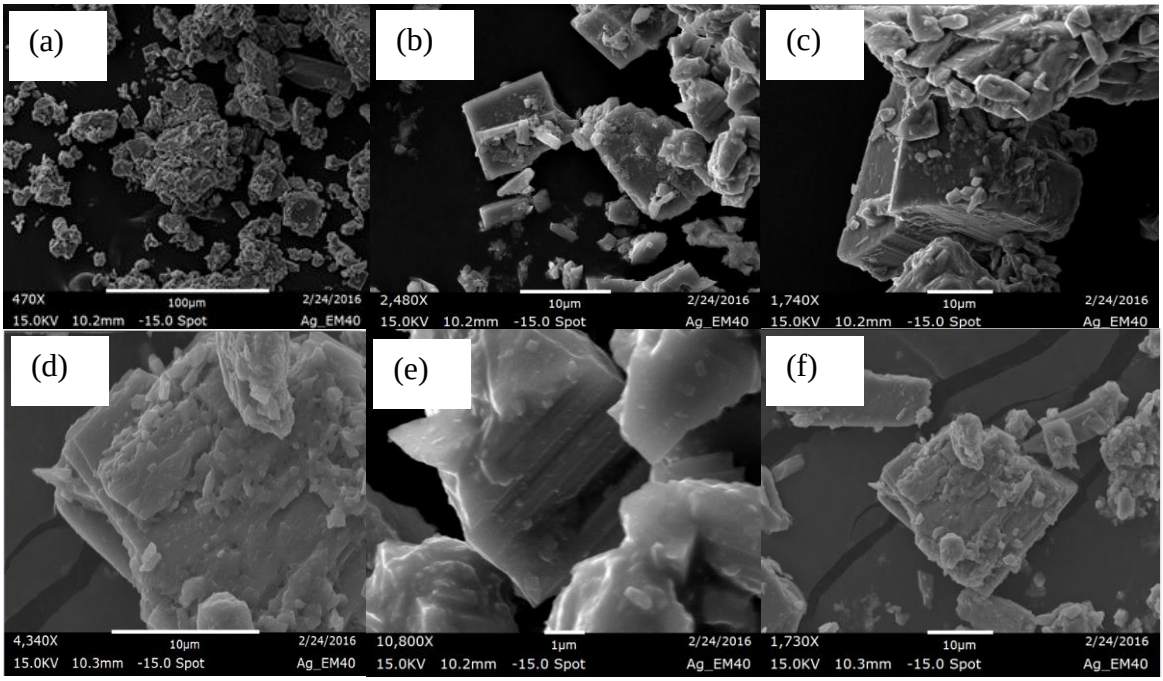

Figure 4.9 SEM micrographs of (a) – (d) solid samples synthesized with H_2O_2/Mo = 6.5 and P/Mo = 1. Scale bars are 100 µm for (a), 1 µm for (b) and 10 µm for (c), (d), (e) and (f)

SEM images in **Figure 4.9 (a) – (f)** reveal particles range in sizes 10 – 120 µm. No difference in the surface textures was observed in SEM images. The SEM images show particulates which are not flat but ones that contain a significant thickness. All the

particulates visible in the SEM images are of similar rectangular shape and corresponds with the optical micrographs.

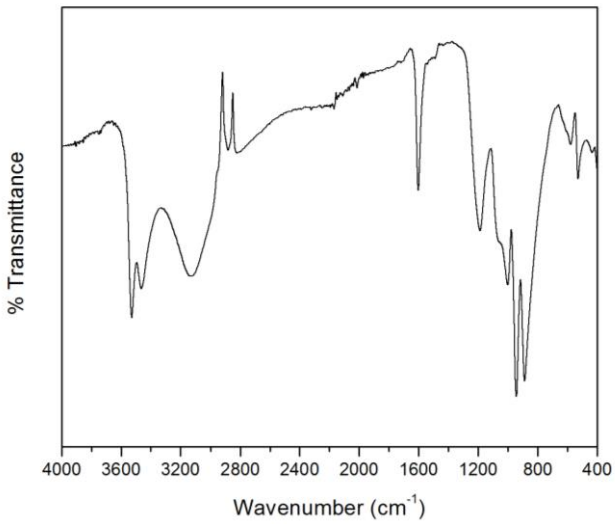

Figure 4.10 ATR-FTIR spectrum of final purified product; H_2O_2/Mo = 6.5, P/Mo = 1

The presence of structural tetrahedral phosphate groups and molybdenum atoms in octahedral environments could be further evidenced using the ATR-FTIR spectrum of the final purified product (H_2O_2/Mo = 6.5, P/Mo = 1; **Figure 4.10** and **Table 3**).[83] The ATR-FTIR spectrum consist of peaks corresponding to stretching vibrations of phosphate ions in the structure (ν = 574 cm^{-1}; ν = 1050 cm^{-1}, ν_{as} = 1194 and 1597 cm^{-1}; ν_s = 874 cm^{-1} and ν = 1008 cm^{-1}).[84,87] The spectrum also reveals the bending and stretching vibrations corresponding to Mo–O bonds in MoO_6 octahedral units in the double chain crystal structure (δ = 574 cm^{-1}; ν_{as} = 936 cm^{-1}).[83,88,89] Peaks between 2815 – 3530 cm^{-1} belong to stretching vibrations of O–H bonds of H_2O present in the molybdenum phosphate structure (ν = 2816, 2878, 3126, 3457, 3529 cm^{-1}).[84,87–89]

Table 3 IR peaks and peak assignments for the final molybdenum phosphate product; H_2O_2/Mo = 6.5, P/Mo = 1

IR peaks (cm^{-1})	Peak assignments
523	-
574	ν P–O and δ O–Mo–O
874	ν_s P–O–H
936	ν Mo–O
1008	ν P–O
1050	ν P–O
1194, 1597	ν_{as} O–P–O
2816, 2878, 3126, 3457 and 3529	ν O–H of H_2O

* ν – stretching vibrations, ν_s – symmetric stretching vibrations, ν_{as} – asymmetric stretching vibrations, δ – bending vibrations.[83,84,87–89]

The Raman spectrum (**Figure 4.11** and **Table 4**) of the final product confirms the peaks shown in the ATR-FTIR spectrum. Raman peak ranges that fall between 340 – 440 cm^{-1}, 515 – 630 cm^{-1}, 870 – 910 cm^{-1}, 930 – 980 cm^{-1}, 988 – 1020 cm^{-1}, 1060 – 1101 cm^{-1} and 1120 – 1170 cm^{-1} correspond to stretching vibrations of P–O of PO_4 tetrahedral units.[77–82,85,86] Peak ranges 870 – 910 cm^{-1}, 930 – 980 cm^{-1} and 988 – 1020 cm^{-1} can be assigned to Mo–O stretching vibrations of MoO_6 octahedral units in the one-dimensional double

chain crystal structure. External modes of P–O of PO_4 correspond to peaks between 40 – 140 cm^{-1} and 140 – 240 cm^{-1}.[77–82,85,86]

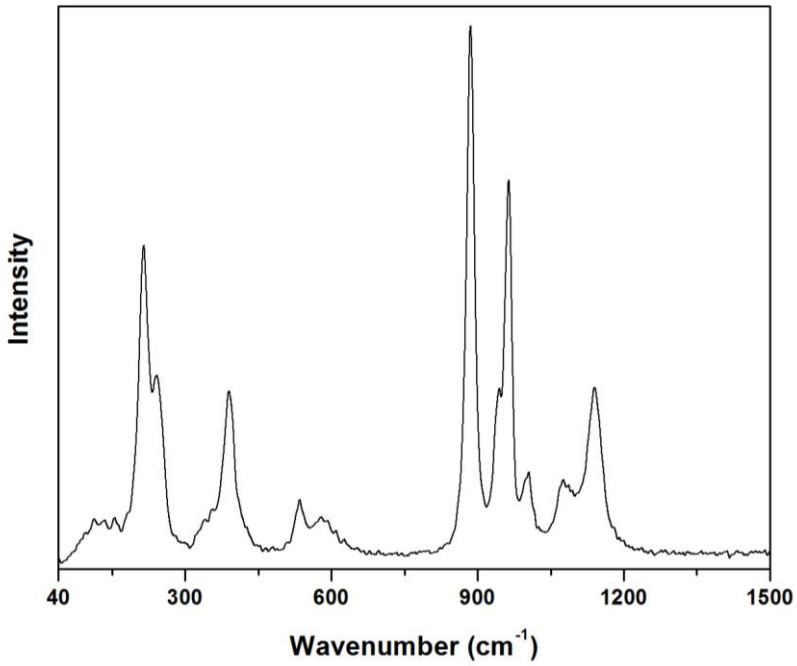

Figure 4.11 Raman spectrum of the final product synthesized; H_2O_2/Mo = 6.5, P/Mo = 1

Table 4 Raman peaks and peak assignments for the final molybdenum phosphate product; H_2O_2/Mo = 6.5, P/Mo = 1

Raman peak range (cm^{-1})	Peak assignments
40 – 140	Weak external modes of PO_4, δ O–Mo–O
140 – 240	External modes, δ O–Mo–O
340 – 440	ν P–O
515 – 630	ν P–O
870 – 910	ν P–O, ν Mo–O
930 – 980	ν P–O, ν Mo–O
988 – 1020	ν P–O, ν Mo–O
1060 – 1101	ν P–O, γ H–O–H
1120 – 1170	ν P–O

* ν – stretching vibrations and δ – bending vibrations.[77–82,85,86]

4.5 Identification of Water Dissolved Species of $MoO_2(H_2O)(HPO_4)$

As $MoO_2(H_2O)(HPO_4)$ completely dissolved in DI water, further studies were conducted to analyze the dissolved species. It was initially speculated that the double chain structures of $MoO_2(H_2O)(HPO_4)$ may be present in water as deprotonated anionic species. In order to capture the dissolved species, inorganic and/or organic cationic species were

introduced to the aqueous solution to induce precipitation of crystals containing both the dissolved molybdenum phosphates species and the counter cations. The precipitation of water-dissolved species of $MoO_2(H_2O)(HPO_4)$ was carried out using 0.500 M solution of $MoO_2(H_2O)(HPO_4)$ and 0.100 M CsCl solution. Other attempts of precipitation, were conducted using 0.100 M $AgNO_3$ solution, 0.100 M CTAB solution (CTAB: cetyl trimethylammonium bromide, 98%, Alfa Aesar) and organic liquids such as pyridine (99%, Alfa Aesar), 4-vinylpyridine (95%, Sigma-Aldrich), 2,6-di-tertbutylpyridine (≥ 97%, Sigma-Aldrich), 1,3-dimethyl-2-imidazolidinone (reagent grade, Alfa Aesar), pyrrole-2-carboxaldehyde (98%, Sigma-Aldrich), 2-picolylamine (99%, Sigma-Aldrich) and 1-(4-aminobutyl)guanidine (97%, Alfa Aesar).

$MoO_2(H_2O)(HPO_4)$ has a high solubility (2 M) in water and produced a yellowish-green solution. Its dissolution was tested also in organic solvents, such as anhydrous methanol (99.8%, Sigma-Aldrich), methanol (99.8%, BDH-VWR analytical), ethanol (200 proof, KOPTEC), 2-butanol (≥ 99.8%, Sigma-Aldrich), acetone (99.5%, BDH-VWR analytical), DMSO (dimethyl sulfoxide) (≥ 99.5%, Sigma-Aldrich), DMF (dimethylformamide) (Sigma-Aldrich), NMF (N-methylformamide) (99%, Sigma-Aldrich) and acetonitrile (Sigma-Aldrich).

4.6 Materials Synthesis

Typical synthesis of cesium molybdenum phosphate consists of two precursor solutions, which were $MoO_2(H_2O)(HPO_4)$ and CsCl solutions. An aqueous solution of 0.500 M $MoO_2(H_2O)(HPO_4)$ was prepared by dissolving 6.60 g of $MoO_2(H_2O)(HPO_4)$ in 5 ml of deionized water with a magnetic stirring in a 30 ml glass vial. An aqueous solution

of 0.100 M CsCl was prepared by dissolving 0.8418 g of CsCl (Alfa Aesar) in 50 ml of deionized water in a 50 ml volumetric flask. Finally, the cesium molybdenum phosphate samples with $MoO_2(H_2O)(HPO_4)$/CsCl = 10 was synthesized by adding, 2.50 ml of 0.100 M aqueous CsCl solution to 5.00 ml of light yellowish-green $MoO_2(H_2O)(HPO_4)$ aqueous solution, on a magnetic stirrer. The resulting product was filtered, rinsed using deionized water and air dried for 24 hrs to produce a yellow colored solid powder.

Dissolution of $MoO_2(H_2O)(HPO_4)$ was explored where 0.100 g of $MoO_2(H_2O)(HPO_4)$ solid was added to 10 ml of each solvent, methanol, ethanol, 2-butanol, acetone, DMSO, DMF, NMF and acetonitrile, and stirred (using a magnetic stirrer) for 24 hrs. Dissolution of $MoO_2(H_2O)(HPO_4)$, also, in anhydrous methanol was investigated. To 5 ml of anhydrous methanol, 0.6048 g of $MoO_2(H_2O)(HPO_4)$ solid was added to produce a 0.5 M solution. The mixture was continuously stirred using a magnetic stirrer, for 24 hrs and observations were recorded at 3 hrs, 6 hrs, 18 hrs and 24 hrs.

4.7 Materials Characterization

Powder X-ray diffraction (PXRD) patterns were obtained using Siemens D5000 diffractometer that consists of Cu Kα radiation. The ground samples were placed on a zero-background quartz sample holder, and data was acquired by scanning 2θ from 5 to 90° with a step size of 0.0403° and a scan time of 30 min. Unit cell parameters were determined using the HighScore Plus X'Pert Pro software (Version 2.2c (2.2.3)). The zero position of each PXRD pattern was first calibrated with a silicon powder internal standard (a = 5.4301 Å) and the background was subtracted. Scanning electron microscopy (SEM) studies, were performed using a FEI XL-30 Environmental SEM using 5 and 15 keV

electrons, on dry-ground samples. Raman and ATR-FTIR spectra were obtained on a Bruker IFS66V/S spectrophotometer.

4.8 Results and Discussion

Figure 4.12 Final purified dried cesium molybdenum phosphate product; $MoO_2(H_2O)(HPO_4)/CsCl = 10$

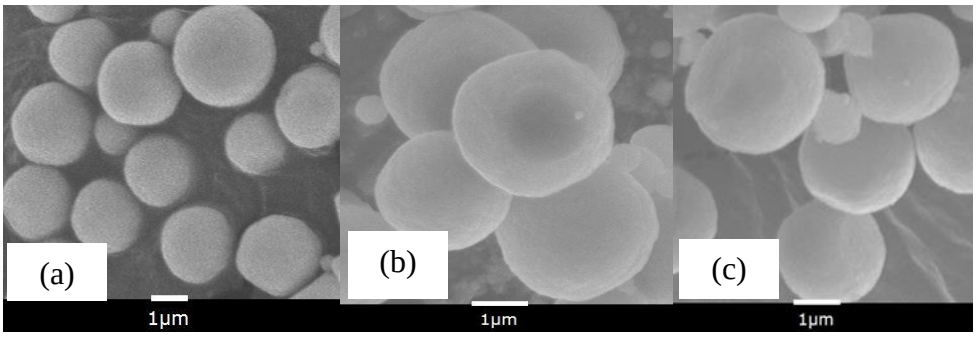

Figure 4.13 SEM micrographs (a) – (c) of cesium molybdenum phosphate products; $MoO_2(H_2O)(HPO_4)/CsCl = 10$. Scale bars are 1 µm for (a) – (c)

Figure 4.12 is a representative photograph of a synthesized cesium molybdenum phosphate sample. The final product is a yellow colored powder. SEM micrographs shown in **Figure 4.13** reveal that, the final products of cesium molybdenum phosphate are spherical particles of size 1 – 5 µm. The surface of spherical particles was homogeneous.

Similar precipitation procedures were followed by using 0.100 M $AgNO_3$ solution, 0.100 M CTAB solution and organic liquid solvents (pyridine, 4-vinylpyridine, 2,6-di-tertbutylpyridine, 1,3-dimethyl-2-imidazolidinone, pyrrole-2-carboxaldehyde, 2-picolylamine and 1-(4-aminobutyl)guanidine). Precipitates of 1,3-dimethyl-2-imidazolidinone ($MoO_2(H_2O)(HPO_4)$/1,3-dimethyl-2-imidazolidinone = 1) was dark bluish brown. The precipitates produced by using $AgNO_3$ [$MoO_2(H_2O)(HPO_4)/AgNO_3$ = 10], CTAB [$MoO_2(H_2O)(HPO_4)$/CTAB = 1], pyridine [$MoO_2(H_2O)(HPO_4)$/pyridine = 1], 2-picolylamine [$MoO_2(H_2O)(HPO_4)$/2-picolylamine = 1], pyrrole-2-carboxaldehyde [$MoO_2(H_2O)(HPO_4)$/pyrrole-2-carboxaldehyde = 1], 1-(4-aminobutyl)guanidine [$MoO_2(H_2O)(HPO_4)$/1-(4-aminobutyl)guanidine = 1] were white in color, while precipitates formed employing 4-vinylpyridine [$MoO_2(H_2O)(HPO_4)$/4-vinylpyridine = 1] and 2,6-di-tertbutylpyridine [$MoO_2(H_2O)(HPO_4)$/2,6-di-tertbutylpyridine = 1] were light yellowish-white in color.

The PXRD patterns (**Figure 4.14**) of purified precipitates of $AgNO_3$, CTAB, 1,3-dimethyl-2- imidazolidinone and pyridine were complicated to analyze. Therefore, precipitation via 0.100 M CsCl solution was attempted. Precipitation was tested using $MoO_2(H_2O)(HPO_4)$/CsCl ratios 5, 8 and 10 which formed bright yellow precipitates. PXRD patterns of $MoO_2(H_2O)(HPO_4)$/CsCl = 5 and 8 were complicated and showed the presence of mixed phase compounds (**Figure 4.14**).

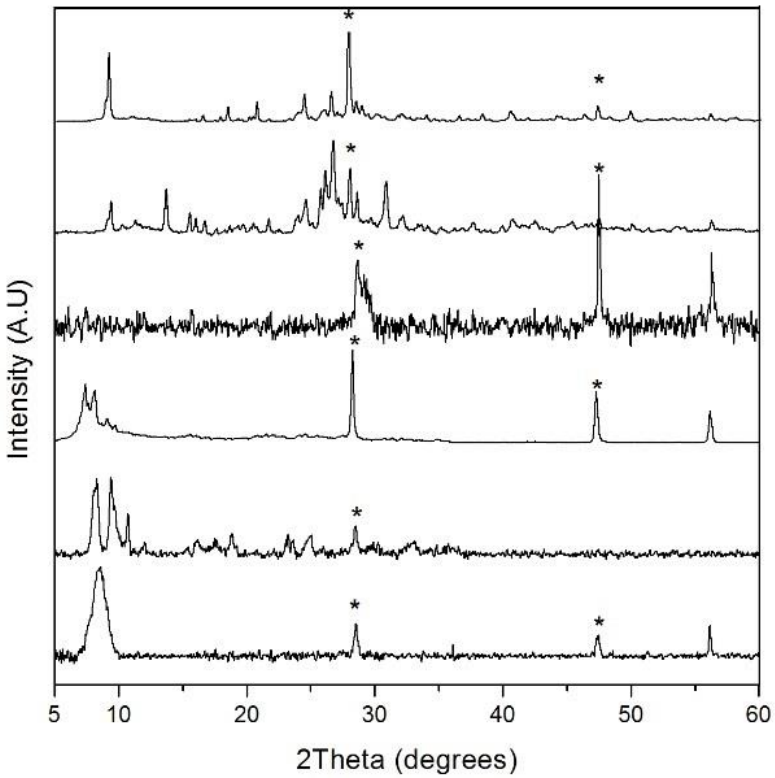

Figure 4.14 PXRD patterns of precipitates with $MoO_2(H_2O)(HPO_4)$/CTAB = 1 (bottom), $MoO_2(H_2O)(HPO_4)$/pyridine = 1, $MoO_2(H_2O)(HPO_4)$/1,3-dimethyl-2-imidazolidinone = 1, $MoO_2(H_2O)(HPO_4)/AgNO_3$ = 10, $MoO_2(H_2O)(HPO_4)$/CsCl = 8 and $MoO_2(H_2O)(HPO_4)$/CsCl = 5 (top). The Bragg peaks of Si (a = 5.4301 Å) are represented by '*'

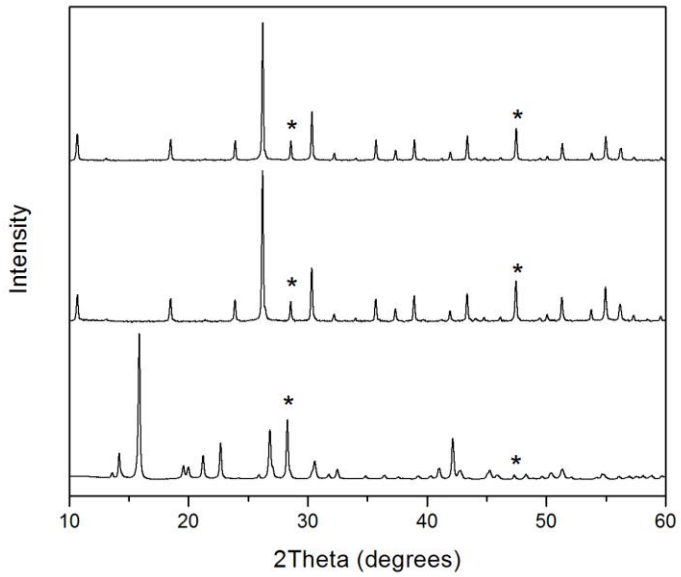

Figure 4.15 PXRD patterns of $MoO_2(H_2O)(HPO_4)$ solid sample (bottom) and samples with nominal $MoO_2(H_2O)(HPO_4)$/CsCl ratio of 10 which have been purified and dried (mid-top). The Bragg peaks of Si (a = 5.4301 Å) are represented by '*'

Figure 4.15 shows the PXRD patterns of a $MoO_2(H_2O)(HPO_4)$ solid sample and two samples with nominal $MoO_2(H_2O)(HPO_4)$/CsCl ratio of 10 which have been purified and dried. The PXRD patterns of the cesium molybdenum phosphate samples revealed the presence of a crystalline compound with higher symmetry. Also, the two patterns from the two cesium molybdenum phosphate samples were identical in peak position and relative intensity. Unit cell dimension refinements were conducted using HighScore Plus X'Pert Pro software (Version 2.2c (2.2.3)). Results of the analysis revealed that the new cesium molybdenum phosphate ($MoO_2(H_2O)(HPO_4)$/CsCl = 10) product has a cubic crystal system, with a primitive (P) Bravais lattice and lattice parameter of 11.8(2) Å. It is worthy stating that the PXRD patterns of the cesium molybdenum phosphate crystalline samples did not correlate to any existing pattern in the ICSD (Inorganic Crystal Structure Database) database on HighScore Plus X'Pert Pro software (Version 2.2c (2.2.3)).

Unfortunately, neither ICP-OES (inductively coupled plasma-optical emission spectrometry) nor EDS (energy-dispersive X-ray spectroscopy) provided consistent and reproducible chemical compositions. Therefore, to accurately identify the functional groups, in the new crystal structure and the water dissolved species of $MoO_2(H_2O)(HPO_4)$, Raman spectroscopic studies were conducted.

As shown in **Figure 4.16 (middle)** the Raman spectrum of 0.500 M $MoO_2(H_2O)(HPO_4)$ aqueous solution was recorded for the peak range 50 – 1300 cm^{-1} (**Table 5**).[78–80,82,85] The peak between 150 – 250 cm^{-1} can be assigned to bending vibrations corresponding to O–Mo–O bonds while, the peak at 325 – 420 cm^{-1} can be assigned to stretching and bending vibrations of the following bonds; P–O and O–Mo–O bonds.[78–80,82,85] The peaks between, 875 – 900 cm^{-1} and 900 – 975 cm^{-1} correspond to stretching vibrations of chemical bonds in the given order; O–Mo–O and P–O bonds, while peak ranges that fall between 50 – 90 cm^{-1} and 90 – 150 cm^{-1} can be assigned to external modes.[78–80,82,85] Further analysis of the Raman spectrum, of the cesium molybdenum phosphate product would confirm the presence of Mo–O and P–O bonds present in the water dissolved species.

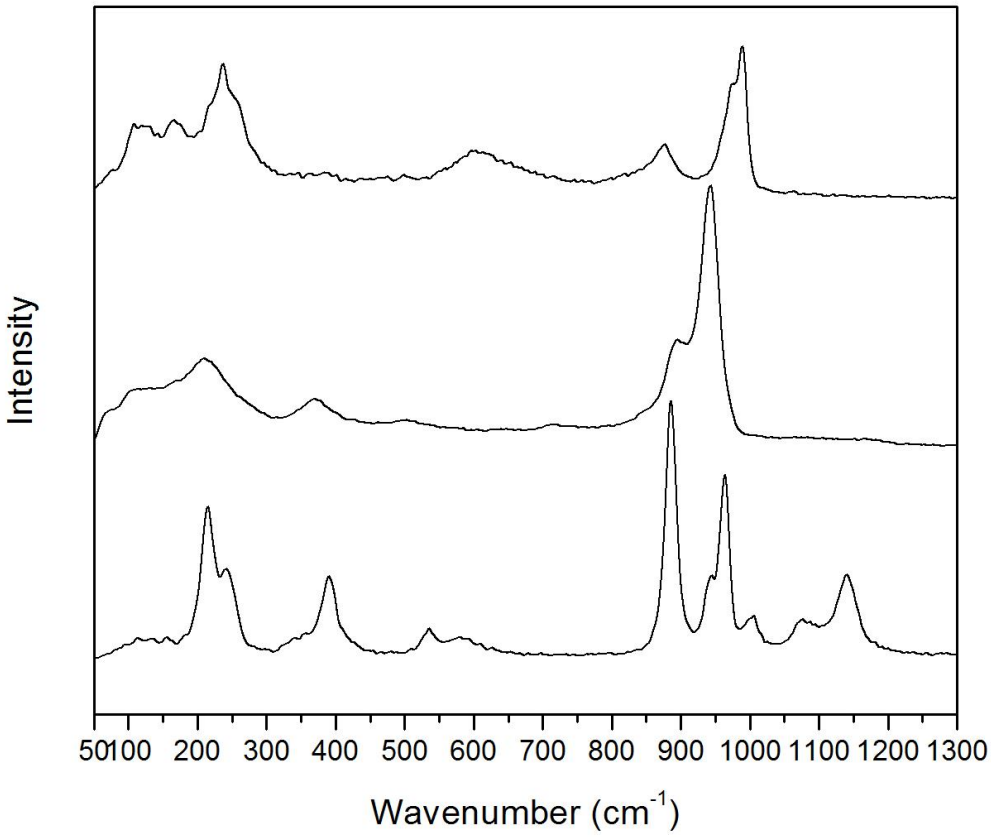

Figure 4.16 Raman spectra of the synthesized $MoO_2(H_2O)(HPO_4)$ solid sample (bottom), 0.500 M $MoO_2(H_2O)(HPO_4)$ aqueous solution (middle) and purified cesium molybdenum phosphate solid sample (top)

Table 5 Raman peaks and peak assignments for 0.500 M $MoO_2(H_2O)(HPO_4)$ aqueous solution

Raman peak range (cm^{-1})	Peak assignments
50 – 90	External modes
90 – 150	External modes
150 – 250	δ O–Mo–O
325 – 420	ν P–O, δ O–Mo–O
875 – 900	ν Mo–O–Mo
900 – 975	ν P–O

* ν – stretching vibrations and δ – bending vibrations.[78–80,82,85]

In **Figure 4.16** (**top**) the Raman spectrum of the cesium molybdenum phosphate product is shown. Within the Raman peak range 40 to 1100 cm^{-1}, it includes peaks positioned at 850 – 900 cm^{-1} and 950 – 1000 cm^{-1}, which can be assigned to both stretching vibrations of P–O bonds and bending vibrations of O–Mo–O bonds (**Table 6**).[77–82,85,86] Peaks between 500 – 700 cm^{-1} correspond to stretching vibrations of P–O bonds while, peaks between 150 – 200 cm^{-1} and 200 – 280 cm^{-1} can be assigned to bending vibrations of O–Mo–O bonds. Finally, peaks at 75 – 150 cm^{-1} correspond with external modes (**Table 6**).[77–82,85,86] The Raman spectrum of the cesium molybdenum phosphate compound confirms the presence of Mo–O bonds and P–O bonds present in its structure as well as in the water dissolved species. However, further analysis of these samples will need to be

conducted to confirm the exact species and its functional groups, present in the 0.5 M $MoO_2(H_2O)(HPO_4)$ aqueous solution.

Table 6 Raman peaks and peak assignments for cesium molybdenum phosphate product; $MoO_2(H_2O)(HPO_4)$/CsCl = 10

Raman peak range (cm^{-1})	Peak assignments
75 – 150	External modes
150 – 200	δ O–Mo–O
200 – 280	δ O–Mo–O
550 – 700	ν P–O
850 – 900	ν P–O, δ O–Mo–O
950 – 1000	ν P–O, δ O–Mo–O

* ν – stretching vibrations and δ – bending vibrations.[77–82,85,86]..

Test results for dissolution of $MoO_2(H_2O)(HPO_4)$ in organic solvents (0.1 g in 10 mL for all the tests) were as follows, complete dissolution of $MoO_2(H_2O)(HPO_4)$ in methanol (not anhydrous; see below) was observed within the first 15 mins and a light yellow solution produced. After 18 hrs of magnetic stirring at RT, complete dissolution of $MoO_2(H_2O)(HPO_4)$ was observed in NMF, resulting a clear solution. However, the dissolution occurs only gradually. After stirring for 24 hrs, incomplete dissolution of $MoO_2(H_2O)(HPO_4)$ was observed in ethanol which resulted a dark blue solution. After 24

hrs, incomplete dissolution was observed in 2-butanol, acetone, DMSO, DMF and acetonitrile with no color change observed in the organic solvent.

Dissolution of $MoO_2(H_2O)(HPO_4)$ (0.6048 g) in anhydrous methanol (5 mL) was investigated. When $MoO_2(H_2O)(HPO_4)$ was added to anhydrous methanol to produce a 0.5 M solution, anhydrous methanol turned bluish and became dark blue after 3 hrs of continuous stirring. After 6 hrs of continuous stirring, about 80% of $MoO_2(H_2O)(HPO_4)$ was dissolved from visual inspection and dark blue color of the solution changed to green/light green, while a white precipitate started forming (**Figure 4.17**). After 18 hrs and 24 hrs a white precipitate in a light green solution was visible.

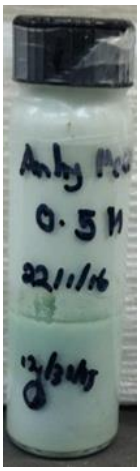

Figure 4.17 Precipitate formed after 24 hrs of stirring a mixture of $MoO_2(H_2O)(HPO_4)$ and an anhydrous methanol solvent (concentration 0.5 M)

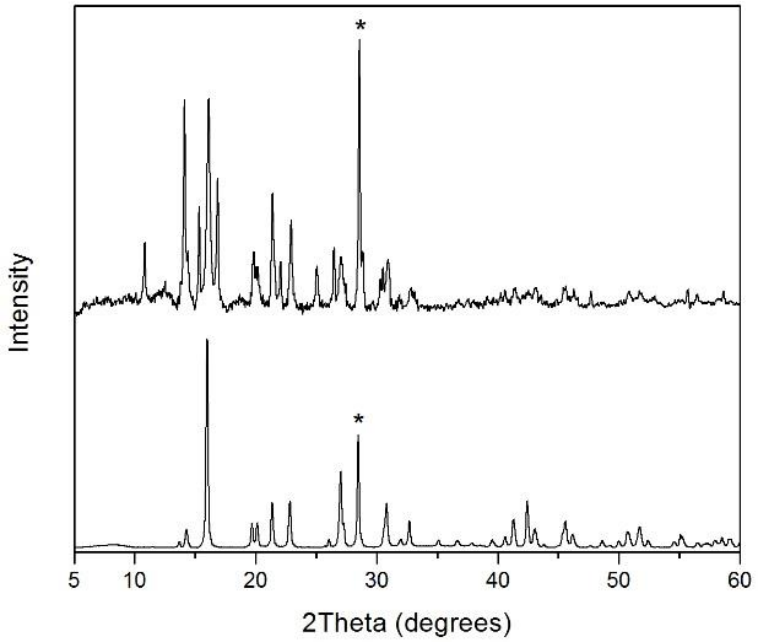

Figure 4.18 PXRD patterns of $MoO_2(H_2O)(HPO_4)$ (bottom) and precipitate resulting from a solution mixture of $MoO_2(H_2O)(HPO_4)$ and anhydrous methanol (0.5 M) (top). The Bragg peaks of Si (a = 5.4301 Å) are represented by '*'

The PXRD pattern of the resulting precipitate is shown in **Figure 4.18** together with that of $MoO_2(H_2O)(HPO_4)$. Peaks at 16°, 31°, 32° and 33° in the pattern of the precipitate match those in the PXRD pattern of $MoO_2(H_2O)(HPO_4)$, indicating the presence of the latter. Peaks at 14.5°, 19.5° – 20°, 21.5°, 23° were found on both PXRD patterns but were stronger in intensity in the PXRD pattern of the $MoO_2(H_2O)(HPO_4)$-anhydrous methanol precipitate. In the $MoO_2(H_2O)(HPO_4)$-anhydrous methanol precipitate PXRD pattern, new Bragg peaks appeared at 11°, 15°, 17°, 22°, 25.5° and 26.5°. These observations suggest the presence of a new chemical compound which probably contain methanol. Further studies were conducted on the precipitate, using ATR-FTIR spectroscopy.

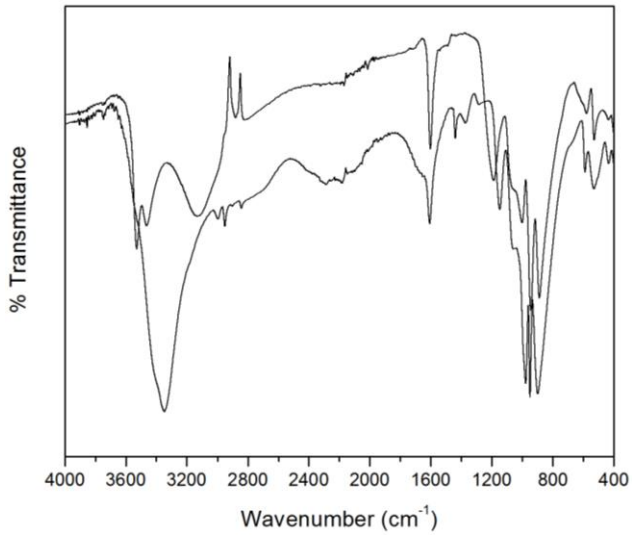

Figure 4.19 ATR-FTIR spectrum of $MoO_2(H_2O)(HPO_4)$ (top) and precipitate formed by mixing $MoO_2(H_2O)(HPO_4)$ and anhydrous methanol to prepare a 0.5 M solution (bottom)

As shown in **Figure 4.19** some of the peaks present in the ATR-FTIR spectrum of $MoO_2(H_2O)(HPO_4)$-anhydrous methanol precipitate, corresponds to IR peaks of the $MoO_2(H_2O)(HPO_4)$ spectrum (**Table 7**). These peaks were broader compared to the peaks in the $MoO_2(H_2O)(HPO_4)$ spectrum and the vibrations corresponded with the following chemical bonds, stretching vibrations of Mo–O bonds (966 cm^{-1}), bending vibrations of O–Mo–O bonds (574 cm^{-1}), stretching vibrations of P–O bonds (584 cm^{-1} and 987 cm^{-1}), symmetric stretching vibrations of P–O–H bonds (895 cm^{-1}), asymmetric stretching vibrations of O–P–O bonds (1142 cm^{-1})and stretching vibrations of O–H of H_2O (3487 – 3115 cm^{-1}).[83,84,87–89]

The peak at 1049 cm^{-1} was assigned to the stretching vibration of C–O bond and the peak at 1431 cm^{-1} corresponds with CH_3 deformation vibration.[90] The CH_3 stretching vibration corresponded with the peak at 2836 cm^{-1}, 2939 cm^{-1}, 2950 cm^{-1} and 2991 cm^{-1}, while the peak at 3343 cm^{-1} was assigned to the stretching vibration of O–H bond.[90] Therefore, the PXRD patterns and ATR-FTIR spectra validates the presence of H_3C-, C–

O- and O–H- groups in the $MoO_2(H_2O)(HPO_4)$-anhydrous methanol precipitate product. It can be speculated that some form of the methanol molecule existed within the double chain structure of $MoO_2(H_2O)(HPO_4)$.

Table 7 Peaks and peak assignments for the precipitate, formed by mixing $MoO_2(H_2O)(HPO_4)$ and anhydrous methanol to produce a 0.5 M solution

IR peaks (cm^{-1})	Peak assignments
584	ν P–O, δ O–Mo–O
895	ν_s P–O–H
966	ν Mo–O
987	ν P–O
1049	ν C–O, ν P–O
1142	ν_{as} O–P–O
1431	CH_3 s-deformation
2836	ν CH_3-s
2950, 2939 and 2991	ν CH_3-d
3343	ν O–H
3115 – 3497	ν O–H of H_2O

* ν – stretching vibrations, ν_s – symmetric stretching vibrations, ν_{as} – asymmetric stretching vibrations, δ – bending vibrations.[83,84,87–90]

The final purified product was imaged using the optical microscope (**Figure 4.20**) to study its morphology. The optical micrographs in **Figure 4.20 (a)** show transparent crystalline particulates whose dimensions are ~ 100 µm. All the crystalline particulates have rectangular shapes with sharp edges and no other crystalline shape is visible. These crystallites were unstable in the presence of moisture in air and started disintegrating within seconds. **Figure 4.20 (b)** shows the point at which the crystallites start absorbing moisture. As shown in **Figure 4.20 (b) – (d)** crystallites start losing its shape and disappearing completely.

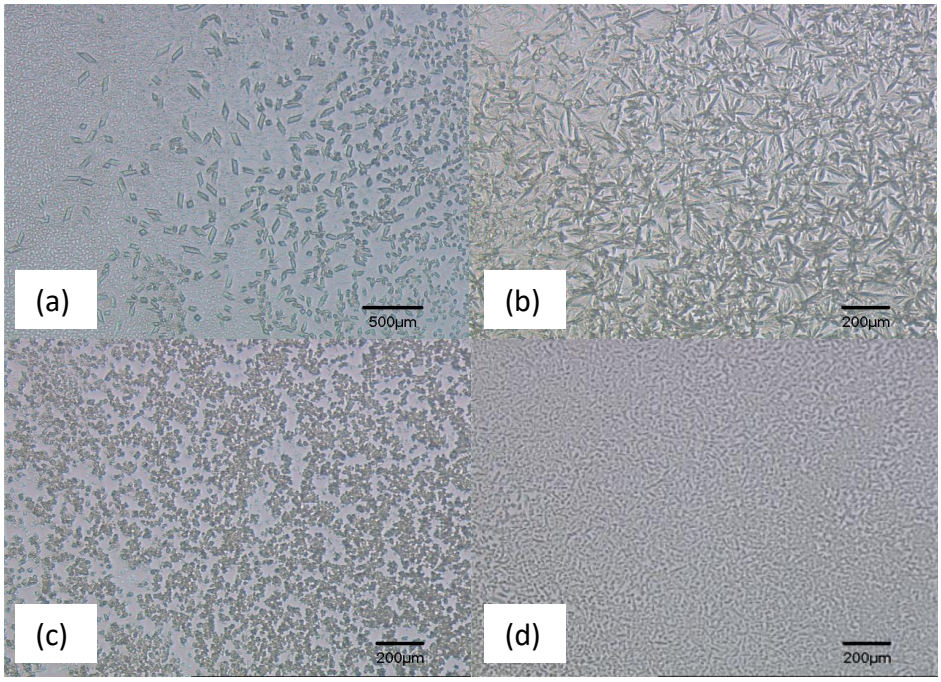

Figure 4.20 Optical micrographs of the precipitate formed by mixing $MoO_2(H_2O)(HPO_4)$ with anhydrous methanol to form a 0.5 M solution (a) – (d). (a) – (d) show the disintegration of crystallites (within 1 min), when exposed to air/moisture. Scale bars are 500 µm for both (a) and 200 µm for (b) – (d)

4.9 Concluding Remarks

A new peroxide based synthetic route was developed to produce $MoO_2(H_2O)(HPO_4)$. The synthesis is unique due to its use of hydrogen peroxide as a stabilizing ligand during preparation of peroxo-molybdenum precursor solutions. While the previous synthesis was carried out under a harsh acidic reaction condition at a high temperature, the novel peroxide method provides the opportunity for the use of lesser number of nonhazardous chemicals, lower drying temperatures and simple experimental procedure. The lower drying temperatures and atomic level mixing of the reactants offer better control of product synthesis which effortlessly led to obtain highly crystalline $MoO_2(H_2O)(HPO_4)$. Overall, the peroxide-based synthetic method is shown to be a greener, inexpensive and energy efficient procedure. Future directions may include utilization of $MoO_2(H_2O)(HPO_4)$ in applications such as acid catalysis and electrocatalysis.

To identify water dissolved species of $MoO_2(H_2O)(HPO_4)$, precipitation of the dissolved species was carried out using a CsCl solution ($MoO_2(H_2O)(HPO_4$)/CsCl = 10). A new cesium molybdenum phosphate compound, with a high symmetry crystal structure was obtained. Further studies may need to be carried out to identify the crystal structure and primary structural units of this product.

REFERENCES

(1) Suchanek, W. L.; Riman, R. E. Hydrothermal Synthesis of Advanced Ceramic Powders. *Adv. Sci. Technol.* **2006**, *45*, 184–193.

(2) Brinker, C. J.; Scherer, G. W. Introduction. In *Sol-Gel Science*; 1990; p xvi-18.

(3) Sol. In *IUPAC Compendium of Chemical Terminology*; IUPAC: Research Triagle Park, NC.

(4) Gel. In *IUPAC Compendium of Chemical Terminology*; IUPAC: Research Triagle Park, NC.

(5) Sá Ferreira, R. A.; Carlos, L. D.; De Zea Bermudez, V. Excitation Energy Dependence of Luminescent Sol-Gel Organically Modified Silicates. *Thin Solid Films* **1999**, *343–344* (1–2), 476–480.

(6) Pagliaro, M.; Ciriminna, R.; Man, M. W. C.; Campestrini, S. Better Chemistry through Ceramics: The Physical Bases of the Outstanding Chemistry of ORMOSIL. *J. Phys. Chem. B* **2006**, *110* (5), 1976–1988.

(7) Styskalik, A.; Skoda, D.; Barnes, C.; Pinkas, J. The Power of Non-Hydrolytic Sol-Gel Chemistry: A Review. *Catalysts* **2017**, *7* (6), 168.

(8) Feng, S. H.; Li, G. H. Hydrothermal and Solvothermal Syntheses. In *Modern Inorganic Synthetic Chemistry: Second Edition*; Elsevier B.V., 2017; pp 73–104.

(9) Jugović, D.; Uskoković, D. A Review of Recent Developments in the Synthesis Procedures of Lithium Iron Phosphate Powders. *J. Power Sources* **2009**, *190* (2), 538–544.

(10) Danks, A. E.; Hall, S. R.; Schnepp, Z. The Evolution of "sol–gel" Chemistry as a Technique for Materials Synthesis. *Mater. Horiz.* **2016**, *3* (2), 91–112.

(11) Jolivet, J. P.; Henry, M.; Livage, J.; Bescher, E. Condensation and Precipitation in Aqueous Solution. In *Metal Oxide Chemistry and Synthesis: Third Edition*; JOHN WILEY & SONS, LTD: England, 1994; pp 25–37.

(12) Mieritz, D. Nanoporous Transparent Conducting Oxides and New Solid Acid Catalysts, Arizona State University, 2016.

(13) Yamabi, S.; Imai, H. Crystal Phase Control for Titanium Dioxide Films by Direct Deposition in Aqueous Solutions. *Chem. Mater.* **2002**, *14* (2), 609–614.

(14) Klementova, M.; Motlochova, M.; Bohaćěk, J.; Kupcí k, J.; Palatinus, L.;

Plizingrova, E.; Szatmary, L.; Sŭbrt, J. Metatitanic Acid Pseudomorphs after Titanyl Sulfates: Nanostructured Sorbents and Precursors for Crystalline Titania with Desired Particle Size and Shape. *Cryst. Growth Des.* **2017**, *17* (12), 6762–6769.

(15) Titanium(IV) oxysulfate ≥29% Ti (as TiO_2) basis, technical | Sigma-Aldrich https://www.sigmaaldrich.com/catalog/product/sial/14023?lang=en&region=US (accessed Sep 27, 2018).

(16) Lencka, M. M.; Riman, R. E. Thermodynamic Modeling of Hydrothermal Synthesis of Ceramic Powders. *Chem. Mater.* **1993**, *5* (1), 61–70.

(17) Gao, Y.; Masuda, Y.; Peng, Z.; Yonezawa, T.; Koumoto, K. Room Temperature Deposition of a TiO_2 Thin Film from Aqueous Peroxotitanate Solution. *J. Mater. Chem.* **2003**, *13* (3), 608–613.

(18) Wang, Z.; Xiao, C.; Yamada, S.; Yoshinaga, K.; Bu, X. R.; Zhang, M. Concentration-Driven Phase Control for Low Temperature Synthesis of Phase-Pure Anatase and Rutile Titanium Oxide. *J. Colloid Interface Sci.* **2015**, *448*, 280–286.

(19) Schwarzenbach, G.; Mühlebach, J.; Müller, K. The Peroxo Complexes of Titanium. *Inorg. Chem.* **1970**, *9* (11), 2381–2390.

(20) Mori, M.; Shibata, M.; Kyuno, E.; Ito, S. Reaction of Hydrogen Peroxide with Titanium (IV) at Different pH Values. *Bull. Chem. Soc. Japan* **1956**, *29* (8), 904–907.

(21) Jagadale, T. C.; Takale, S. P.; Sonawane, R. S.; Joshi, M.; Patil, S. I.; Kale, B. B.; Ogale, S. B.; Joshi, H. M. N-Doped TiO_2 Nanoparticle Based Visible Light Photocatalyst by Modified Peroxide Sol-Gel Method N-Doped TiO_2 Nanoparticle Based Visible Light Photocatalyst by Modified Peroxide Sol - Gel Method. *J. Phys. Chem. C* **2008**, *112* (3), 14595–14602.

(22) Sutradhar, N.; Sinhamahapatra, A.; Kumar Pahari, S.; Bajaj, H. C.; Baran Panda, A. Room Temperature Synthesis of Protonated Layered Titanate Sheets Using Peroxo Titanium Carbonate Complex Solution. *Chem. Commun.* **2011**, *47* (27), 7731–7733.

(23) Kumar, B. V.; Velchuri, R.; Devi, V. R.; Prasad, G.; Sreedhar, B.; Bansal, C.; Vithal, M. Preparation, Characterization, Emission (Eu^{3+}), and Electron Spin Resonance (Gd^{3+}) Studies of $Y_{2-x}Ln_xTi_2O_7$(Ln=Eu and Gd, x=0.0,0.05). *J. Appl. Phys.* **2010**, *108* (4).

(24) Kakihana, M.; Tada, M.; Shiro, M.; Petrykin, V.; Osada, M.; Nakamura, Y. Structure and Stability of Water Soluble $(NH_4)_8[Ti_4(C_6H_4O_7)_4(O_2)_4]\cdot 8H_2O$. *Inorg. Chem.* **2001**, *40* (5), 891–894.

(25) Haight, G. P.; Boston, D. R. Molybdenum Species in Aqueous Solution — A Brief

Summary. *J. Less Common Met.* **1974**, *36* (1), 95–102.

(26) Krishnan, C. V.; Garnett, M.; Hsiao, B.; Chu, B. Electrochemical Measurements of Isoppolyoxometalates: 1. pH Dependent Behavior of Sodium Molybdate. *Int. J. Electrochem. Sci* **2007**, *2*, 29–51.

(27) Ng, K. Y. S.; Gulari, E. Spectroscopic and Scattering Investigation of Isopoly-Molybdate and Tungstate Solutions. *Polyhedron* **1984**, *3* (8), 1001–1011.

(28) Oyerinde, O. F.; Weeks, C. L.; Anbar, A. D.; Spiro, T. G. Solution Structure of Molybdic Acid from Raman Spectroscopy and DFT Analysis. *Inorganica Chim. Acta* **2008**, *361* (4), 1000–1007.

(29) Csanyi, Laszlo J.; Horvath, Istvan; Galbacs, Z. M. Peroxide Derivatives of molybdenum(VI) in Neutral and Alkaline Media. *Transit. Met. Chem* **1989**, *14*, 90–94.

(30) Csányi, L. J. Peroxide Derivatives of Molybdenum (VI) in Acidic Solution. *Transit. Met. Chem.* **1989**, *14* (2), 90–94.

(31) Cruywagen, J. J.; Hevns, J. B. B. Equilibria and UV Spectra of Mono- and Polynuclear Molybdenum(VI) Species. *Inorg. Chem.* **1987**, *26* (16), 2569–2572.

(32) Krishnan, C. V.; Chen, J.; Burger, C.; Chu, B. Polymer-Assisted Growth of Molybdenum Oxide Whiskers via a Sonochemical Process. *J. Phys. Chem. B* **2006**, *110* (41), 20182–20188.

(33) Kurusu, Y. Thermal Behavior of a New Type Molybdenum Oxide Obtained by Oxidation of Molybdenum Powder or Molybdenum Trioxide with Hydrogen Peroxide. *Bull. Chem. Soc. Jpn* **1981**, *54* (1), 293–294.

(34) Segawa, K.; Ooga, K.; Kurusu, Y. Molybdenum Peroxo Complex. Structure and Thermal Behavior. *Bull. Chem. Soc. Jpn* **1984**, *57*, 2721–2724.

(35) Ammam, M. Polyoxometalates: Formation, Structures, Principal Properties, Main Deposition Methods and Application in Sensing. *J. Mater. Chem. A* **2013**, *1* (21), 6291–6312.

(36) Kozhevnikov, I. V. Catalysis by Heteropoly Acids and Multicomponent Polyoxometalates in Liquid-Phase Reactions. *Chem. Rev.* **1998**, *98* (1), 171–198.

(37) Mukhopadhyay, S.; Debgupta, J.; Singh, C.; Kar, A.; Das, S. K. The Otherwise Inactive Keggin Polyoxometalate Becomes Active towards Elecrocatalytic Water Oxidation in Neutral pH:POM@ZIF- 8, an Efficient and Robust Electrocatalyst. *Angew. Chemie Int. Ed.* **2017**, *57*, 7.

(38) Kortz, U.; Jeannin, Y. P.; Tézé, A.; Hervé, G.; Isber, S. A Novel Dimeric Ni-Substituted Beta-Keggin Silicotungstate: Structure and Magnetic Properties of $K_{12}[\{\beta\text{-}SiNi_2W_{10}O_{36}(OH)_2(H_2O)\}_2].20H_2O$. *Inorg. Chem.* **1999**, *38* (16), 3670–3675.

(39) Liu, L.; Li, H.; Dai, J. Photosensitivity in Ce/Sm-Decorated Keggin Polyoxomolybdates: An Interesting Photoinduced Coloration Phenomenon of Mixed-Metal Clusters Involving Energy Transfer from Rare-Earth Fluorescence. *Sci. China Chem.* **2014**, *57* (6), 918–922.

(40) Ikeda, S.; Nishiya, S.; Yamamoto, A.; Yamase, T.; Nishimura, C.; Clercq, E. De. Activity of the Keggin Polyoxotungstate Pm-19 against Herpes Simplex Virus Type 2 Infection in Immunosuppressed Mice: Role of Peritoneal Macrophage Activation. *J. Med. Virol.* **1993**, *41* (3), 191–195.

(41) Wang, X.; Wang, J.; Zhang, W.; Id, B. L.; Zhu, Y.; Hu, Q. Inhibition of Human Immunodeficiency Virus Type 1 Entry by a Keggin Polyoxometalate. *Viruses* **2018**, *10* (Mvc), 265.

(42) Marosi, L.; Platero, E. E.; Cifre, J.; Arean, C. O. Thermal Dehydration of $H_{3+x}PV_xM_{12-x}O_{40}\cdot yH_2O$ Keggin Type Heteropolyacids; Formation, Thermal Stability and Structure of the Anhydrous Acids $H_3PM_{12}O_{40}$, of the Corresponding Anhydrides $PM_{12}O_{38.5}$ and of a Novel Trihydrate $H_3PW_{12}O_{40}\cdot 3H_2O$. *J. Mater. Chem.* **2000**, *10* (8), 1949–1955.

(43) Yang, G. P.; Dilixiati, D.; Yang, T.; Liu, D.; Yu, B.; Hu, C. W. Phosphomolybdic Acid as a Bifunctional Catalyst for Friedel–Crafts Type Dehydrative Coupling Reaction. *Appl. Organomet. Chem.* **2018**, *32* (9), 1–6.

(44) Sadakane, M.; Steckhan, E. Electrochemical Properties of Polyoxometalates as Electrocatalysts. *Chem. Rev.* **1998**, *98* (1), 219–238.

(45) Da Silva, M. J.; Teixeira, M. G. An Unexpected Behavior of $H_3PMo_{12}O_{40}$ Heteropolyacid Catalyst on the Biphasic Hydrolysis of Vegetable Oils. *RSC Adv.* **2017**, *7* (14), 8192–8199.

(46) Catalytic and Structural Studies of Some Heteropoly Acids and Polyoxometalates Part I Laxmikant D. Chavan Page 1; pp 1–32.

(47) Journal, A. Epoxidation of Some Olefins with Hydrogen Peroxide Catalyzed by Heteropolyoxometalates. *Asian J. Chem.* **2008**, *20* (1), 8–14.

(48) Chauhan, A. Powder XRD Technique and Its Applications in Science and Technology. *J. Anal. Bioanal. Tech.* **2014**, *5* (6).

(49) Pecharsky, V. K.; Zavalij, P. Y. *Fundamentals of Powder Diffraction and Structural*

Characterization of Materials; Springer, 2005.

(50) Mariani, M. M.; Deckert, V. Raman Spectroscopy : Principles , Benefits , and Applications. **2018**, 421–460.

(51) Ferraro, J. R.; Nakamoto, K.; Brown, C. W. *Introductory Raman Spectroscopy*; Academic Press, 2003.

(52) Chase, B. FT–Raman Spectroscopy: A Catalyst for the Raman Explosion. *J. Chem. Educ.* **2007**, *84* (1), 75.

(53) Matsui, T.; Kukino, T.; Kikuchi, R.; Eguchi, K. An Intermediate Temperature Proton-Conducting Electrolyte Based on a CsH_2PO_4/SiP_2O_7 Composite. *Electrochem. Solid-State Lett.* **2005**, *8* (5), A256–A258.

(54) Hibino, T.; Kobayashi, K.; Nagao, M.; Shinji, K. High-Temperature Supercapacitor with a Proton-Conducting Metal Pyrophosphate Electrolyte. *Sci. Rep.* **2015**, *5* (7903), 1–7.

(55) Wang, R.; Ye, J.; Rauf, A.; Wu, X.; Liu, H.; Ning, G.; Jiang, H. Microwave-Induced Synthesis of Pyrophosphate $Zr_{1-x}Ti_xP_2O_7$ and TiP_2O_7 with Enhanced Sorption Capacity for Uranium (VI). *J. Hazard. Mater.* **2016**, *315*, 76–85.

(56) Maârouf, I.; Oulmekki, A.; Toyir, J.; Nawdali, M.; Zarguili, I.; Ghadraoui, H. El. Development of New $Zr_XTi_{1-X}P_2O_7$ Materials as Model Compounds for the Recycling of Metallic Waste from Phosphate Chemistry. **2017**, *7* (8), 2807–2815.

(57) Meng, X.; Hao, M.; Shi, J.; Cao, Z.; He, W.; Gao, Y.; Liu, J.; Li, Z. Novel Visible Light Response Ag_3PO_4/TiP_2O_7 composite Photocatalyst with Low Ag Consumption. *Adv. Powder Technol.* **2017**, *28* (3), 1047–1053.

(58) Singh, B.; Bhardwaj, A.; Gautam, S. K.; Parkash, O.; Kumar, D.; Jadhav, H. S.; Song, S. J. Synthesis and Characterization of MnO-Doped Titanium Pyrophosphates ($Ti_{1-x}Mn_xP_2O_7$; X = 0–0.2) for Intermediate-Temperature Proton-Conducting Ceramic-Electrolyte Fuel Cells. *Ionics (Kiel).* **2017**, *23* (7), 1675–1684.

(59) Wu, W.; Shanbhag, S.; Wise, A.; Chang, J.; Rutt, A.; Whitacre, J. F. High Performance TiP_2O_7 Based Intercalation Negative Electrode for Aqueous Lithium-Ion Batteries via a Facile Synthetic Route. *J. Electrochem. Soc.* **2015**, *162* (9), A1921–A1926.

(60) Senguttuvan, P.; Rousse, G.; Oró-Solé, J.; Tarascon, J. M.; Palacín, M. R. A Low Temperature TiP_2O_7 Polymorph Exhibiting Reversible Insertion of Lithium and Sodium Ions. *J. Mater. Chem. A* **2013**, *1* (48), 15284.

(61) Shi, Z.; Wang, Q.; Ye, W.; Li, Y.; Yang, Y. Synthesis and Characterization of

Mesoporous Titanium Pyrophosphate as Lithium Intercalation Electrode Materials. *Microporous Mesoporous Mater.* **2006**, *88* (1–3), 232–237.

(62) Levi, G.; Peyronel, G. Crystal Structure of the Isomorphous Group MP_2O_7. *Zeitschrift Für Krist.* **1935**, *92*, 190–209.

(63) Durif, A. Crystal Chemistry of Condensed Phosphate; Springer Science & Business Media. **2013**, 49–52.

(64) Norberg, S. T.; Svensson, G.; Albertsson, J. A TiP_2O_7 Superstructure. *Acta Crystallogr. Sect. C Cryst. Struct. Commun.* **2001**, *57* (3), 225–227.

(65) Scientific, E.; Company, P.; Ginestra, A. L. A. On the Existence of Pyropiiosi'i-Iates Metals Having a Layered Structure of Tetravalent. **1982**, *58*, 179–189.

(66) Baker, A. R. Synthesis and Characterisation of Novel Metal Pyrophosphates. **2014**, No. September, 1–197.

(67) Hibino, T.; Shen, Y.; Nishida, M.; Nagao, M. Hydroxide Ion Conducting antimony(V)-Doped Tin Pyrophosphate Electrolyte for Intermediate-Temperature Alkaline Fuel Cells. *Angew. Chemie - Int. Ed.* **2012**, *51* (43), 10786–10790.

(68) Imanaka, N.; Masui, T.; Hirai, H. Stabilization of Amorphous Titanium Pyrophosphate by Niobium or Tantalum Doping. *J. Mater. Sci.* **2005**, *40* (12), 3309–3311.

(69) Kierkergaard, P. On the Crystal Structure of $MoO_2(PO_3)_2$. *Ark. kemi* **1962**, *18*, 521–532.

(70) Wen, B.; Chernova, N. A.; Zhang, R.; Wang, Q.; Omenya, F.; Fang, J.; Whittingham, M. S. Layered Molybdenum (Oxy)pyrophosphate as Cathode for Lithium-Ion Batteries. *Chem. Mater.* **2013**, *25* (17), 3513–3521.

(71) Lister, S. E.; Soleilhavoup, A.; Withers, R. L.; Hodgkinson, P.; Evans, J. S. O. Structures and Phase Transitions in $(MoO_2)_2P_2O_7$. *Inorg. Chem.* **2010**, *49* (5), 2290–2301.

(72) Uebou, Y.; Okada, S.; Yamaki, J. I. Electrochemical Insertion of Lithium and Sodium into $(MoO_2)_2P_2O_7$. *J. Power Sources* **2003**, *115* (1), 119–124.

(73) Lister, S. E.; Rixom, V. J.; Evans, J. S. O. Structural and Mechanistic Studies of the Dehydration of $MoO_2PO_3OH{\cdot}H_2O$ and the In Situ Identification of Two New Molybdenum Phosphates. *Chem. Mater.* **2010**, *22* (18), 5279–5289.

(74) Kierkergaard, P. On the Crystal Structure of $(MoO_2)_2P_2O_7$. *Ark. kemi* **1962**, *19*, 1–14.

(75) Deng, W.; Feng, X.; Xiao, Y.; Li, C. Layered Molybdenum (Oxy) Pyrophosphate $(MoO_2)_2P_2O_7$ as a Cathode Material for Sodium-Ion Batteries. *Chemelectrochem* **2018**, *5* (7), 1032–1036.

(76) Kierkergaard, P. The Crystal Structure of $Mo(OH)_3PO_4$. *Acta Chem. Scand.* **1958**, *12*, 1701–1714.

(77) Frost, R. L.; Scholz, R.; López, A.; Xi, Y. A Vibrational Spectroscopic Study of the Phosphate Mineral Whiteite $CaMn^{++}Mg_2Al_2(PO_4)_4(OH)_2{\cdot}8(H_2O)$. *Spectrochim. Acta - Part A Mol. Biomol. Spectrosc.* **2014**, *124*, 243–248.

(78) G.D. Saraivaa, J.A. Lima Jrb, F.F. de Sousac, J.H. da Silvad, V. O. S. N.; A.J. Ramiro de Castrob, J. M. F. Pressure Dependent Raman Studies in the $K_2Mo_2O_7.H_2O$ Crystal. *Vib. Spectrosc.* **2018**, *94* (1), 89–94.

(79) Mestl, G.; Ilkenhans, T.; Spielbauer, D.; Dieterle, M.; Timpe, O.; Krohnert, J.; Jentoft, F.; Knozinger, H.; Schlogl, R. Thermally and Chemically Induced Structural Transformations of Keggin-Type Heteropoly Acid Catalysts. *Appl. Catal. a-General* **2001**, *210* (1–2), 13–34.

(80) Aatiq, A.; Marchoud, A.; Bellefqih, H.; Tigha, M. R. Structural and Raman Spectroscopic Studies of the Two $M_{0.50}SbFe(PO_4)_3$ (M = Mg, Ni) NASICON Phases. *Powder Diffr.* **2017**, *32* (S1), S40–S51.

(81) Szumera, M. Molybdenum Modified Phosphate Glasses Studied by31P MAS NMR and Raman Spectroscopy. *Spectrochim. Acta - Part A Mol. Biomol. Spectrosc.* **2015**, *137*, 111–115.

(82) Stefov, V.; Koleva, V.; Najdoski, M.; Abdija, Z.; Cahil, A.; Šoptrajanov, B. Vibrational Spectra of $Mg_2KH(XO_4)_2{\cdot}15H_2O$ (X = P, As) Containing Dimer Units $[H(XO_4)_2]$. *Spectrochim. Acta - Part A Mol. Biomol. Spectrosc.* **2017**, *183*, 387–394.

(83) Weller, M. .; Bell, R. . PROTON MOBILITY AND THE STRUCTURE OF $MoO_2HPO_4.H_20$. *Solid State Ionics* **1989**, *35*, 79–84.

(84) Jiang, G.; Qiao, J.; Hong, F. Application of Phosphoric Acid and Phytic Acid-Doped Bacterial Cellulose as Novel Proton-Conducting Membranes to PEMFC. *Int. J. Hydrogen Energy* **2012**, *37* (11), 9182–9192.

(85) Isaac, M.; Pradip, T.; Nayar, V. . Infrared and Polarized Raman Spectra of $(C_5H_7N_2)_6Mo_7O_{24}.3H_2O$. *J. Solid State Chem.* **1994**, *112*, 132–138.

(86) Quesada Cabrera, R.; Firth, S.; Blackman, C. S.; Long, D. L.; Cronin, L.; McMillan, P. F. Spectroscopic Studies of Sulfite-Based Polyoxometalates at High Temperature and High Pressure. *J. Solid State Chem.* **2012**, *186*, 171–176.

(87) Mazari, T.; Cadot, E.; Rabia, C. Preparation and Characterization of Keggin-Type Heteropolysalts, $Co_X PMo_{12} O_{40}$ (X = 0–1.5). *MATEC Web Conf.* **2013**, *5*, 4022.

(88) Wang, X. J.; Nesper, R.; Villevieille, C.; Novák, P. Ammonolyzed MoO_3 Nanobelts as Novel Cathode Material of Rechargeable Li-Ion Batteries. *Adv. Energy Mater.* **2013**, *3* (5), 606–614.

(89) Phuruangrat, A.; Jitrou, P.; Dumrongrojthanath, P.; Ekthammathat, N.; Kuntalue, B.; Thongtem, S.; Thongtem, T. Hydrothermal Synthesis and Characterization of Bi_2MoO_6 Nanoplates and Their Photocatalytic Activities. *J. Nanomater.* **2013**, 1–8.

(90) Methyl Alcohol https://webbook.nist.gov/cgi/cbook.cgi?ID=C67561&Type=IR-SPEC&Index=28#IR-SPEC (accessed Oct 21, 2018).